

A SIMULATION SCHEME TO INVESTIGATE THE ROLE OF STIFFNESS GRADIENT ALONG THE BODY COLUMN OF HYDRA



A thesis submitted towards partial fulfilment of
MS Degree Programme

by


DEVANSHU SINHA


under the guidance of

DR. APRATIM CHATTERJI
ASSOCIATE PROFESSOR, DEPT. OF PHYSICS
INDIAN INSTITUTE OF SCIENCE EDUCATION AND RESEARCH
PUNE

Certificate

This is to certify that this thesis entitled "A simulation scheme to investigate the role of stiffness gradient along the body column of Hydra" submitted towards the partial fulfilment of the MS degree programme at the Indian Institute of Science Education and Research Pune represents original research carried out by "Devanshu Sinha" at "Indian Institute of Science Education and Research", under the supervision of "Dr. Apratim Chatterji" during the academic year 2016-2019.

 Date: 23/July/2020
Student
DEVANSHU SINHA


Supervisor
DR. APRATIM
CHATTERJI

Declaration

I hereby declare that the matter embodied in the report entitled “A simulation scheme to investigate the role of stiffness gradient along the body column of Hydra” are the results of the investigations carried out by me at the Department of Physics, IISER Pune, under the supervision of Dr. Apratim Chatterji and the same has not been submitted elsewhere for any other degree.



Student

DEVANSHU SINHA

Date 23/July/2020



Supervisor

DR. APRATIM
CHATTERJI

Acknowledgements

I would like to thank my supervisor Dr. Apratim Chatterji for continued support during course of my research. He always made sure we had all the resources at our disposal which accelerated the research, including high performance computing clusters, and a strong guidance. He always found time for us even during holidays for any discussion or help.

I would like to thank our collaborators: Suyash Naik, Manu Unni, Sha-truhan Singh Rajput, P. Chandramouli Reddy, Dr. Shivprasad Patil and Dr. Sanjeev Galande, who did all the experimental work on Hydra, including the AFM measurements and analysis. All the AFM measurements were done in Dr. Shivprasad Patil, while Hydra was cultured and hypothesis validation experiments were conducted in Dr. Sanjeev Galande's lab.

For the additional work on shear banding in the last chapter of this thesis, I would like to thank Alex Abraham. I have used the model and simulation code developed initially by Alex and Dr. Apratim for the shear banding simulations.

I am also grateful to my fellow lab members, particularly Tejal for her guidance as my senior.

Abstract

Animals have evolved a variety of features that help them to move in different media, like air, water or land. Such features usually develop such that the finite amount of energy available to the animals is utilized more efficiently. Hydra is one such animal, which has a diverse set of mechanisms for locomotion, including looping, swaying and somersault. It has a small (about 5 mm) tubular shaped body with tentacles at one end. Hydra belongs to the phylum of Cnidaria, which were the earliest phylum to evolve differentiated neuronal/muscular tissues and extracellular matrix (ECM) properties.

The motivation for the thesis comes from the experiment conducted in Dr. Shivprasad Patil's lab, by Suyash Naik, Manu Unni and Shatruhan Singh Rajput. In this experiment, an AFM (Atomic Force Microscope) was used to produce a spatially resolved map of tissue elasticity along the Hydra's body column. It was observed that Hydra polyps have a three times higher stiffness in first 25% of their body column than the rest (the stiffness ratio of 3 : 1). A careful examination of Hydra's motion led to the hypothesis by Dr. Shivprasad Patil that the stiffness gradient of 3 : 1 may help Hydra utilise its stored energy more efficiently during its somersault motion, compared to a Hydra with no stiffness variation.

In this thesis, we propose a coarse grained computer simulation model, to investigate the link between Hydra's somersault and the observed stiffness gradient. We explore the energetics the somersault motion by analysing the dynamics of action-reaction forces like viscous drag, gravity, buoyancy in our simulations. We also compare and contrast other stiffness ratios and attempt to understand if there is a special significance of the ratio 3 : 1.

The last chapter of the thesis is dedicated to some additional work done on the topic of Shear banding in wormlike Micelles. In this chapter, we report preliminary results of first time observation of the phenomena of shear banding in a wormlike micellar system, using molecular dynamics simulations.

Contents

1 Introduction and Experimental overview	4
1.1 Thesis outline	7
1.2 Motivation: Why study Hydra's somersault?	8
1.3 Measurement of Hydra's elasticity using Atomic Force Microscopy	8
1.4 Chemical Perturbation To Mitigate ECM Stiffness	12
1.5 Physical Perturbation To Mitigate ECM Stiffness	12
1.6 Video analysis of somersault	14
1.7 Estimation of Hydra's density	16
2 Computational and Theoretical model of Hydra and its validation	17
2.1 Bead-spring Model of Hydra	18
2.2 Response to axial deformation of model-Hydra	19
2.3 Implementation of external forces	20
2.4 Time evolution of model-Hydra: Damped velocity verlet algorithm	24
2.5 Visual comparison of model-Hydra with real Hydra videos	25
2.6 Simulation units	26
2.7 Initial setup and objective of the simulations	30
3 Simulation results and discussion	33
3.1 Basal tip height versus time plots and Relaxation time	34
3.2 Total Potential and Kinetic energy with time	37
3.3 Energy and Momentum of basal and shoulder region	37
3.4 Average force at the junction	40
3.5 Estimation of the Threshold Energy ($E_{Threshold}$)	41
3.6 Stored energy in the shoulder after contraction $E_{shoulder}$ versus time (t)	42
3.7 Density difference ($\Delta\rho$) versus α : Phase Plots	43

4 Conclusion and Remarks	47
4.1 Future perspective, drawbacks of the model and experiments	48
5 Additional work: Molecular Dynamics simulation scheme to study shear banding in worm-like micelles	50
5.1 Introduction	50
5.2 Chapter outline	52
5.3 Details of the Simulation Model	53
5.4 Simulations	55
5.4.1 System initialization and equilibration	55
5.4.2 Application of strain rate	55
5.5 Result and discussions	59
5.6 Conclusion and future perspective	59
References	61
A Exponential nature of bending energy E_{bend} with Time (t)	65
B Velocity Verlet algorithm in Damped condition	68
C $E_{shoulder}$ versus time (t) for $\epsilon = 0.2$ and $\epsilon = 1.1$	70
D Maxwell's model for Viscoelasticity	71
D.1 Stress relaxation under constant strain of $\gamma_{yx}(t) = \gamma_{yx}^0$	72
D.2 Stress relaxation under oscillatory strain: Strain of $\gamma_{\theta\phi} = \gamma_{\theta\phi}^0 \sin(\omega t)$	73
D.3 Stress relaxation under oscillatory strain rate: Strain rate of $\dot{\gamma}_{\theta\phi} = \dot{\gamma}_{\theta\phi}^0 \sin(\omega t)$	75

Chapter 1

Introduction and Experimental overview

As a result of millions of years of evolution, animals have developed multiple different ways to move through aquatic, terrestrial, fossorial, as well as aerial media. Many animals have also developed abilities to move across two or more different media, for example, a Brown Pelican can completely submerge itself in water from mid-flight, and fly again directly from the ocean surface [\[1\]](#).

Locomotion is defined as the process of moving from one place to another. Animals use locomotion for many different reasons, such as running from predators, looking for mate, searching for food, or changing their micro-habitat. Locomotion is also not always an active process like swimming, hopping, running etc. Some animals depend on their environment for locomotion. For example, a species of tiny beetles called *N. kronaueri*, recently discovered in the jungles of Costa Rica have the ability to attach themselves on top of army ants to move [\[2\]](#). Such type of locomotion is known as “passive locomotion” [\[3\]](#).

The energetics of locomotion is governed primarily by the action-reaction forces of Newton’s third law. An animal needs to overcome multiple different types of forces in order to move, such as viscous drag, gravitation, inertia etc. The magnitude of these forces depend on the medium and the animal’s size, for example viscous drag is much higher in water than on land.

In general, all forms of locomotion require energy, which is not available for other efforts. Animals thus tend to progressively evolve features that utilize energy with increasing efficiency over multiple generations [\[4\]](#).

There are also cases where such an efficient use of energy is not optimal, and the priority is given to performance. An example of such a case could be running away from predators.

Animals also don't always tend to use only a single form of locomotion. Some animals tend to use more than one way to move, depending upon the situation. For example, a wheel spider, which would otherwise move using its legs, escapes Pompilid wasps by turning to its side and cartwheeling down the sand dunes [5].

Some animals also use a mixture of active and passive forms of locomotion at the same time, while at other times use a purely passive, or a purely active form of motion. An example of such an animal is Hydra.

Hydra is a small fresh water organism that belongs to the class of Hydrozoa and the phylum Cnidaria. They have a long cylindrical body column about 5 mm in length. Hydra's body wall is composed of two cell layers [6],[7] (called the epithelial cells) separated by a thin, structure-less layer of connective tissue called the Mesoglea (fig 1.1).

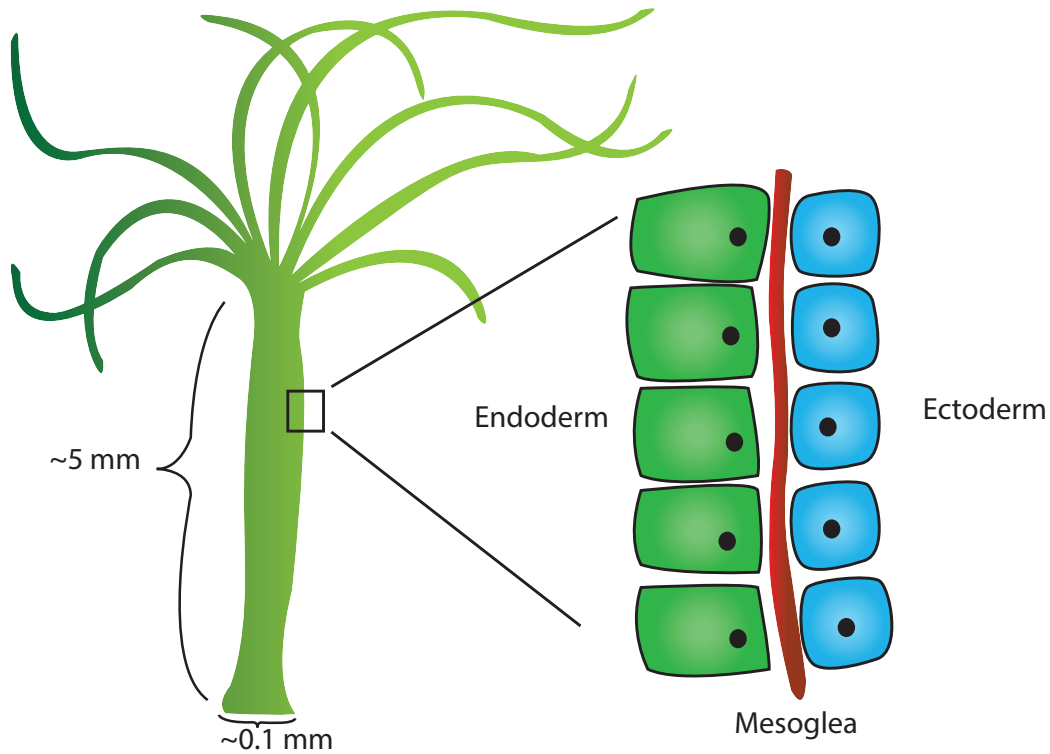


Figure 1.1: Hydra is typically observed to be around 5 mm in length and 0.1 mm in diameter. The Hydra cell wall is composed of a Mesoglea, which is sandwiched between the Endoderm and Ectoderm cells.

Just like other animals discussed, Hydras show a variety of methods for locomotion. They utilize passive locomotion by generating small air bubbles in their basal disc and float along the water current [8]. They destroy

the bubble once they reach their favourable location. They also show more complex movements such as swaying, looping and somersault.

In looping, the Hydra extends and attaches to the substrate using its tentacles, and then drags its base close to the hypostome. It then proceeds to detach its tentacles with the base firmly attached to the new position on the substratum. Somersault (fig 1.2) is slightly different than looping, in that it involves adhering to the substrate with the tentacles for traction. The body is moved around the head in a semi-circular arc, with characteristic contractions.

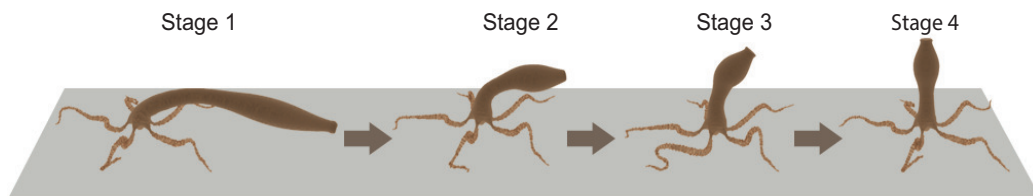


Figure 1.2: Hydra's somersault motion is shown as a four stage process. The first two stages consists of contraction from a stretched state. This is achieved by the detachment of basal-tip, which is initially adhered to the substrate. The later two states show the upward motion of the basal tip, which moves the Hydra body in an inverted position.

The focus of this thesis, is to investigate the energetics of the somersault motion. This investigation was motivated by a peculiar Young's modulus variation observed along the body column of Hydra using an atomic force microscopy (AFM).

The elasticity, or the Young's modulus of the Hydra is largely controlled by the ECM which is sandwiched between its two cells (fig 1.1). Hydra polyp was attached to a substrate, and the Young's modulus along its body column was measured using an AFM. A sharp stiffness gradient was observed, with the top 25% of its body column having a stiffness roughly three times the rest (fig 2.3). As discussed previously, animals have been known to evolve certain physical features which leads to a more efficient utilization of energy during locomotion, as its an energy intensive process. Having made this observation, and also noting the fact that Hydra's somersault motion always involves rising up with the stiffer end firmly placed on the substrate, led us to investigate a possible link between this Young's modulus ratio 3 : 1 between the head and the basal region of Hydra, and its somersault motion.

In particular, it was hypothesized that having a stiffness gradient leads to a more efficient energy storage and utilization during the somersault motion of Hydra. This thesis is a review of experiments and computer simulations

conducted to validate this hypothesis, and understand the significance of such a stiffness gradient in Hydra.

1.1 Thesis outline

The first chapter of the thesis includes, from section 1.3 onwards, a brief overview of all the experiments conducted in the labs of Dr. Shivprasad Patil and Dr. Sanjeev Galande, by Suyash Naik, Manu Unni, Shatruhan S. Rajput and P. Chandramouli Reddy. Section 1.3 summarises how the AFM measurements were conducted and the result of the measurement, which showed a stiffness gradient with a ratio of 3 : 1 along the body column of Hydra. In the two subsequent sections, we review the chemical and physical perturbations done to the hydra, to make its stiffness uniform. This was done to check if the our hypothesis was valid, and if Hydra is able to perform the locomotion with a uniform stiffness.

In the section 1.6 we explore the question of Hydra’s rising up motion being passive or active. We attempt to answer this by looking at the trend of the bending energy dissipation curve. We end chapter 1 with section 1.7, where we review an experiment done to measure the density of Hydra by letting it fall in a long, thin water column, and using Bernoulli’s equations.

To understand the energetics of somersault, and to explore the significance of this special value of Young’s modulus ratio of 3 : 1, we developed a physics based computer simulation scheme. Chapter 2 begins with the introduction to this simulation scheme. Subsequent sections in chapter 2 lay the groundwork for the model’s validation and discuss its scope. After validating the model, we make a qualitative, visual comparison of the somersault motion between a real Hydra and the Hydra generated from our simulations in section 2.5. In the section on units after this (sec 2.6), we establish the final connection between the real world Hydra and the simulations on a quantitative basis. We develop mathematical equations and tables which help us translate between the numbers in the simulations and the real world.

Having validated the model and the units of the simulation in chapter 2, we present the analysis to validate the hypothesis using the simulation model in chapter 3. In sections 3.1 3.2 and 3.3 we compare the simulation model with a uniform stiffness with the one with the experimental value of stiffness gradient ratio. We track the energy stored in the shoulder and the basal region separately and check if the energy storage and dissipation is more efficient in the experimentally observed case. We carry out our initial analysis without the presence of gravity or buoyancy, and also initialise all our comparison cases of simulation at the same potential energy. In sec 3.4

we show that the average force exerted from the basal end to the stiffer shoulder region is higher in the cases where stiffness gradient is present. We also note in the subsequent sections that when we put in the experimentally observed values of Hydra density, the case with the uniform stiffness is unable to complete its somersault, thus reproducing the experimental results. We also discuss the link between Hydra’s density and the stiffness ratio of 3 : 1 by using phase plots in section 3.7. In this chapter, we were able to establish to some extent the importance of having a stiffness gradient ratio, and how it is a massive improvement over just having a uniform gradient. We also establish that the ratio should be between two to six ($\alpha \in [2, 6]$), for optimal energy storage and transfer.

In chapter 4 we summarize our results and discuss some drawbacks of our simulations and experiments (sec 4.1). We provide some insights into how the simulations could be refined further in the future, and how the scope of current simulations can be improved by further analysis.

The simulations, modelling and analysis was conducted in the lab of Dr. Apratim Chatterji, by Devanshu Sinha, Dr. Apratim Chatterji and Dr. Shivprasad Patil.

1.2 Motivation: Why study Hydra’s somersault?

Animals have evolved several features over multiple cycles of evolution, to optimally use their energy for movement. One such trait is the evolution of differentiated neuronal/muscular tissues and extracellular matrix (ECM).

Cnidarians were the earliest phylum to evolve these features. Investigating how the differential stiffness, generated by the ECM, is responsible for the movement of Hydra may improve our understanding of how more complex organisms developed their musculoskeletal systems.

Additionally, the need of an optimal elasticity variation for greater energy efficiency in liquid environments could be a significant design principle for building artificial machines and advance the field of the untethered small-scale robots working in confined areas [9].

1.3 Measurement of Hydra’s elasticity using Atomic Force Microscopy

Most organisms use tissues of different elastic properties in different parts of their body, which helps in an efficient energy storage and consumption

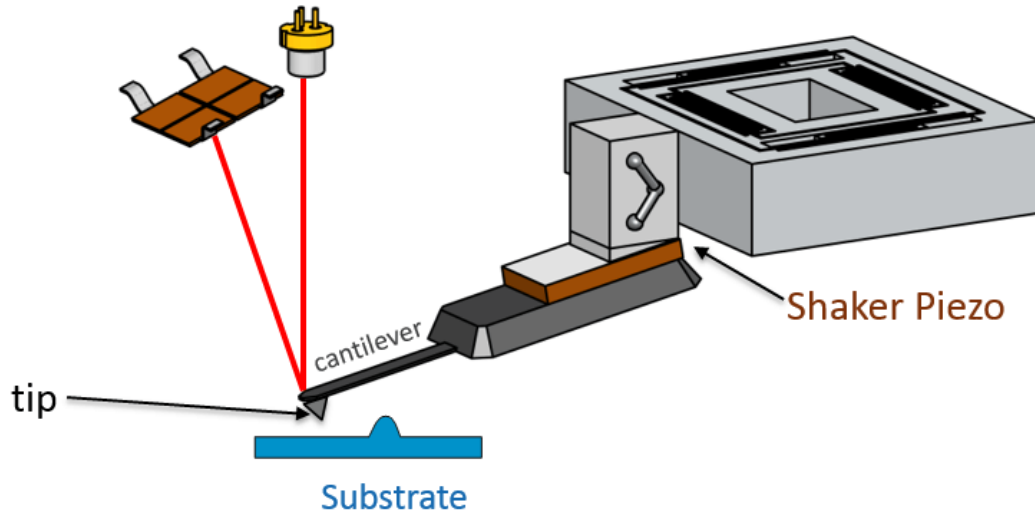


Figure 1.3: An AFM consists of a cantilever, which is attached to a Piezo. The top of the cantilever is coated with a material which reflects a laser beam to a photodetector. As the cantilever moves along the substrate, the beam is deflected due to the forces between the cantilever tip and the substrate. The movement of the laser beam, tracked by the photodetector, reveals the surface topology. Source: <https://www.nanosurf.com/> (Used with permission of Dr. Sujit K Dora, Application Scientist, Nanosurf)

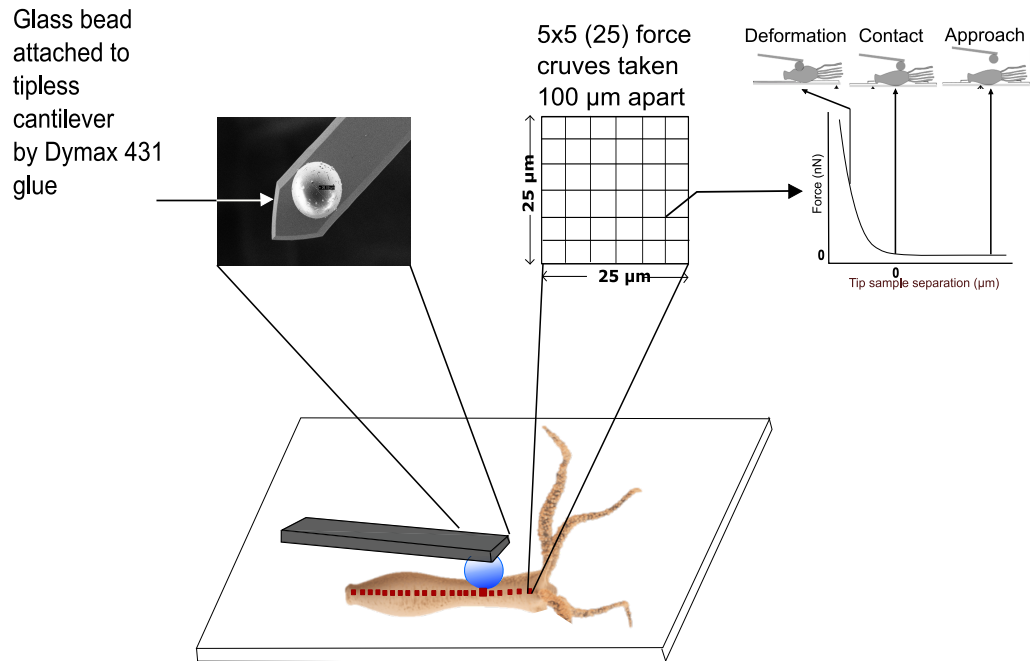
during the locomotion [10], [11]. For example, exoskeleton in invertebrates and musculoskeletal systems in the vertebrates.

The different stiffness properties exhibited by these tissues help in locomotion. Since Hydra uses multiple complex mechanisms for its locomotion, we wanted to investigate if it also shows some kind of spatial variation of stiffness along its body column.

To measure such a spatial variation in detail along Hydra's body column, an atomic force microscope was used. An Atomic Force Microscope, or an AFM, consists of a cantilever attached to shaker. The cantilever, at its other end has a sharp tip that interacts with the substrate in different ways, depending upon the properties which need to be measured. The tip end of the cantilever also consists of a reflective surface at the top/up side, to reflect a laser beam while it raster scans the substrate. The deflections of this laser beam can be measured via a position sensitive photodetector, which picks up the vertical and lateral motion of the probe. The photodetector's deflection sensitivity is calibrated in terms of the nanometers of motion versus the measured voltage (fig 1.1)

A tip-less cantilever, with a spherical glass bead glued to it at the end

A



B

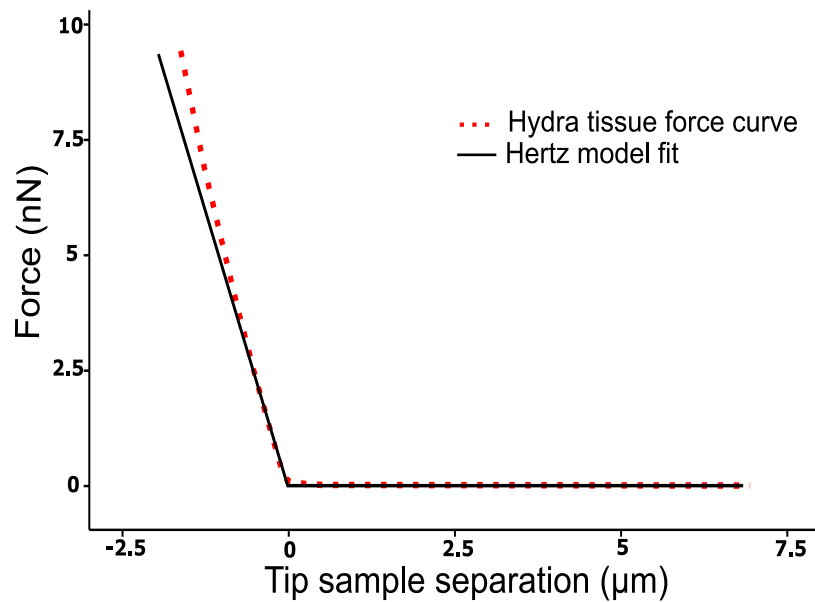


Figure 1.4: **A.** The cantilever tip raster scans along the hydra body column. The zoomed in image of the cantilever has a glass bead attached to it using Dynax-431 glue. **B.** Shows a sample force versus tip and substrate separation curve obtained from the AFM and its fit with the Hertz model

was used to measure the elastic properties of Hydra. A glass bead, instead of a sharp tip is generally used in a cantilever when we measure the elastic properties of the substrate, instead of mapping the microscopic surface.

The glass bead is pushed on the surface of the body column of the hydra, thus deforming it. This deformation curve is fitted with the Hertz model, to extract the elastic moduli (the Young's modulus in our case) of the part of the body column being deformed.

Hertz contact mechanics model can only be used when the nature of the elastic contact is non-adhesive. This means that in order to justify the use of Hertz model, we needed to check if the deformation curve followed any kind of hysteresis. It was observed that this was not the case, thus validating the use of Hertz model.

The AFM measurements of Young's modulus along the Hydra's body column (fig 1.5) showed a very peculiar character. We observed that the Young's modulus was not uniform along the body column, but it was on an average the upper quarter of the body column had thrice the stiffness of the rest.

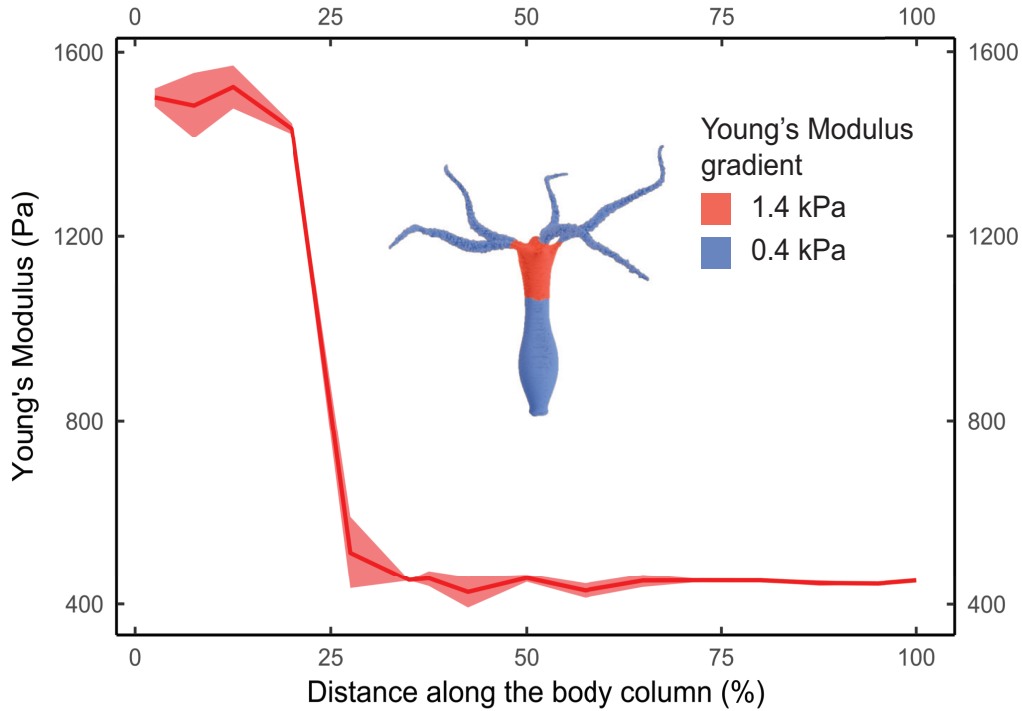


Figure 1.5: Young's modulus measured along the body column of the Hydra varies with the distance along its body column. The top 25 % of the Hydra's body column shows a three times higher stiffness than the rest

Motivated by these experimental studies, it was hypothesized this stiffness gradient plays an important role in the second half of Hydra’s somersault motion (fig 1.2). To investigate this hypothesis further, Hydra’s regenerative property was exploited. Using chemical and physical perturbation, Hydra’s ECM, which is primarily responsible for its stiffness, was destroyed and compared with the Hydra with the stiffness gradient. These experiments are reviewed in the next section.

1.4 Chemical Perturbation To Mitigate ECM Stiffness

To understand the role of stiffness gradient along the body column of Hydra for its locomotion, we need to compare a regular hydra (with a stiffness gradient) with the one without a stiffness gradient. For this, Hydra’s regenerative properties were exploited. It is known that 2,2’-Dipyridyl (DP) is a chemical which inhibits ECM polymerization in Hydra [12], [13], [14], [15]. In the chemical perturbation experiments, Hydra polyps were treated with DP for a time of 72 hours. AFM measurements of Hydra polyps after 72 hours of DP treatment showed that Hydra had a uniform stiffness throughout their body column, as opposed to having a stiffness gradient.

Interestingly, it was also observed that there were zero events of Hydra polyps showing their somersault. This gave the first indication that there could be a possible correlation between Hydra’s ability to somersault and the stiffness gradient along its body.

After a further 36 hours, it was observed that the somersault movement had started again. This also correlates well with the fact that at this time, the stiffness gradient along the Hydra’s body column had been restored to its original value.

1.5 Physical Perturbation To Mitigate ECM Stiffness

Another method used to remove the stiffness gradient was to physically nick the shoulder region. This nick destroys the ECM in the shoulder region, but due to the regenerative nature of Hydra, it starts to heal and restore its stiffness. AFM measurements showed that the stiffness in the shoulder region becomes the same as the rest of the body after 12 hours.

It was observed that the polyps showed a similar behaviour to the chem-

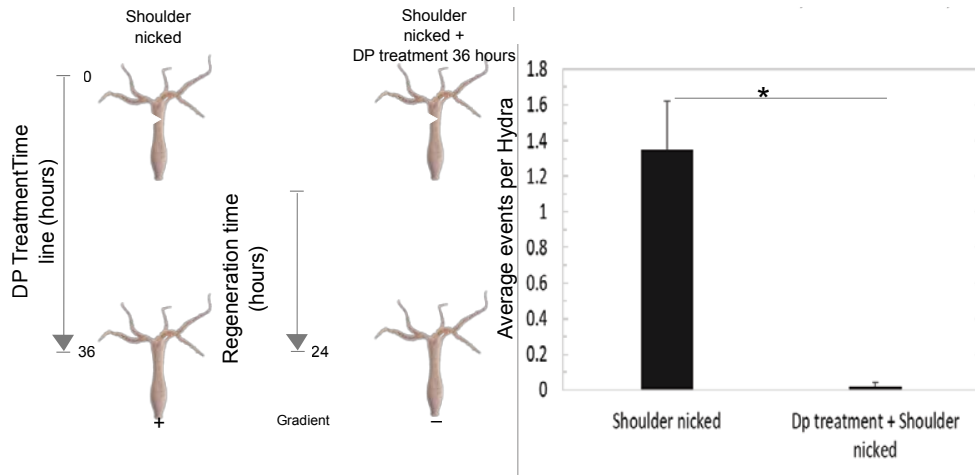


Figure 1.6: The ECM was perturbed globally using chemical disruption of collagens by treatment with 10 mM Dipyrldyl (DP). The treatment time in DP is shown along the arrow. The average somersault events per Hydra reduce upon treatment with DP for 36 hours and none are observed after treatment with DP for 72 hours. The error bars represent standard errors and the significance values are calculated using the 2-tailed paired student's t-test. P-value <0.05 is shown as *, <0.005 is shown as **.

ical perturbation method. No somersault events were recorded when the Hydra had a uniform gradient, thus further indicating towards the hypothesis may have some validity to it.

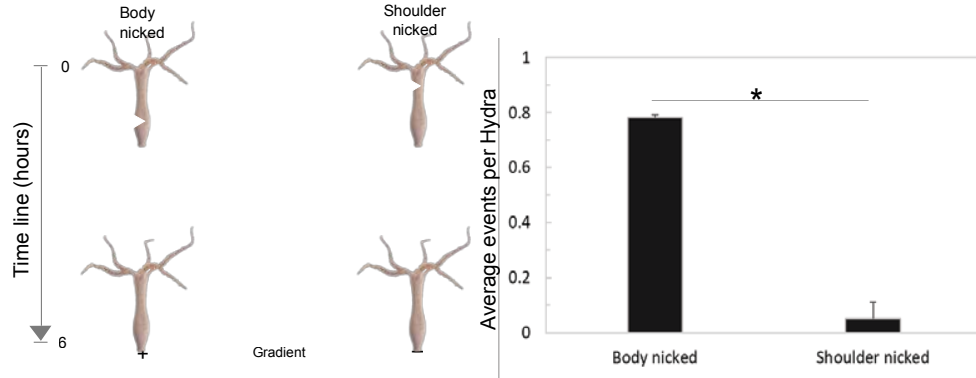


Figure 1.7: The ECM was perturbed locally in Hydra polyp using a partial cut (nick) and the stiffness gradient was abolished (represented as + for native state and – for abolished). The time for regeneration after the nick is shown along the arrow and the nick is represented at the appropriate position along Hydra. The graph shows the average somersault events per Hydra with nicks at the shoulder or the body column (n=20, N=3). Perturbing the stiffness in the shoulder region significantly reduces the somersaults by Hydra polyps. The error bars represent standard errors and the significance values are calculated using the 2-tailed paired student’s t-test. P-value <0.05 is shown as *, <0.005 is shown as **.

1.6 Video analysis of somersault

The physical and chemical perturbations show that a stiffness gradient is indeed required for the Hydra to complete its motion. However, the exact reason for this is still unclear. We discuss this in more details in our simulations. Hydra’s locomotion involves both active and passive components. While the initial stretching part is considered active, the contraction consists of both active and passive parts. The passive part being the stored potential energy which Hydra has due to the initial stretching.

In this section, we review at a basic experiment done to partially answer this question, and confirm to some degree that the contraction and standing inverted is mostly passive.

When the Hydra polyp undergoes the contraction, the potential energy released is composed of two parts. The first part is stored in the stretched part, while the rest is stored in the bent segment which has the higher stiffness. Using careful analysis of high definition video recordings of Hydra as it undergoes the contraction, we can reveal how this stored bending energy behaves with time.

This was done by utilizing the fact that the bending energy is directly proportional to the square of the curvature in the bent region. Using the formula (eq [1.1](#) and [1.2](#)) for bending energy of hollow rods [\[16\]](#) with inner and outer radii, we can extract this energy stored in the bent region.

$$U = \frac{YIL}{2R^2} \quad (1.1)$$

Where,

$$I = \int y^2 dA = \frac{\pi(r_1^2 - r_2^2)}{64} \quad (1.2)$$

Here Y is the Young's modulus, I is the second area moment of Inertia, r_1 and r_2 are the inner and outer radii of the hydra body, L is the length of the bent region and R is the radius of curvature of the bent segment (head region) at any given time.

All other parameters like the stiffness, length etc are mostly fixed, except for the radius of curvature, which evolves with time during Hydra's motion.

This radius of curvature was extracted by fitting Hydra's bent region with carefully calibrated circles using the Fiji software at different time frames. The resulting curve (fig [1.8](#)) shows that the stored energy in the bent region

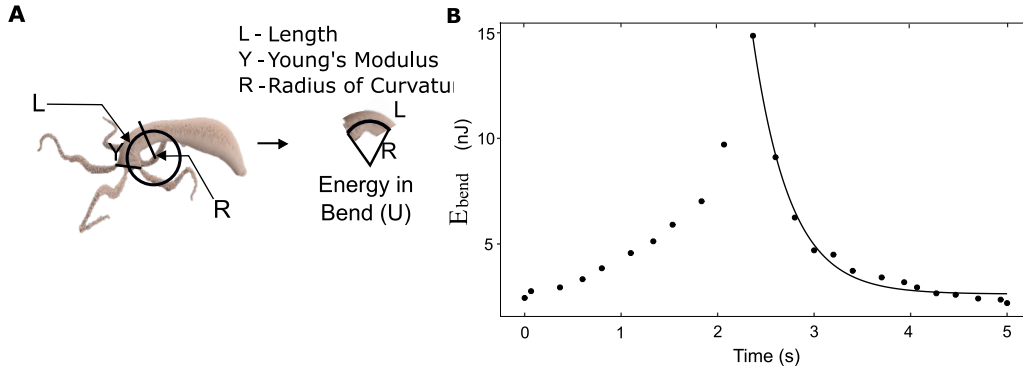


Figure 1.8: **A** Bending energy stored in the shoulder region can be estimated by calculating its curvature. The curvature is calculated using the least square circle fit in every frame of the video, using Fiji software. **B** The experimental data (dots) is shown to fit well with the exponential decay function (solid line)

shows an exponential dissipation. This is consistent with the curve a regular non-living object would show, thus indicating towards the argument that the contraction and standing upright motion of Hydra should be mostly passive, unless Hydra actively tries to conform to an exponential dissipation curve, which is unlikely. For simulations of the same, refer to appendix [A](#)

1.7 Estimation of Hydra's density

Hydra's density determines the extent to which the gravitational force is cancelled out by water's buoyancy. As we shall see in the last chapter, this is crucial to explain the elasticity gradient of Hydra.

The density of Hydra was determined by removing its tentacles and dropping it in a vertical long water column (height 2m, diameter 5cm). When Hydra polyp is dropped in this water column, it attains a terminal velocity which is measured to be $0.003m/s$. It moves downwards horizontally, without rotating or tumbling. At this terminal velocity, we can write a force balance equation (Bernoulli's equation) which yields the following

$$\rho = \rho_0 + \frac{[4\pi\eta L/\ln(L/D)] \times v}{Vg} \quad (1.3)$$

Where ρ is the density of Hydra, ρ_0 and η are density and viscosity of water respectively. L is the length of Hydra body column, D is the diameter of the body column and V is the volume of Hydra and g is the acceleration due to gravity. The length and the diameter of hydra was measured at five different locations across its body column and also measured for 10 different animals. The errors in the measurement of L and D largely determine the errors in estimating the density of Hydra from the measurements. The density of hydra tissue is calculated to be . This is $5 \pm 1.5\%$ above the density of water.

Chapter 2

Computational and Theoretical model of Hydra and its validation

To develop a more in-depth understanding of the underlying mechanics of Hydra's somersault motion, we attempted to develop a physics-based model of Hydra, which captures passive part of the somersault motion.

In our simulations, we simplify Hydra as a hollow elastic cylinder with a given radius, and an elasticity gradient along its body column. The stiffer segment of this "model" Hydra adheres to a substrate while the other end is released from an initial stretched-bent position.

Our simulation's primary goal was to explain how the stiffness gradient helps in locomotion by using the minimum number of input parameters. These parameters are classified into two types, 1. External, and 2. Internal. The external parameters are the parameters of the environment in which the Hydra polyp lives in. These include things like gravity and water's viscosity. The internal parameters for us are things like the dimensions of Hydra (its inner, outer radii, length, etc), Young's modulus of its body column. There are also some derived parameters which couple the external and internal and thus dictate the motion of Hydra; one example would be the Drag coefficient, which results from the multiplication of Hydra's dimensions and water's viscosity, up to some constant.

In this section, we begin by describing the bead-spring network model of Hydra, followed by the model validation studies conducted to see if the results make sense. We end this section by showing a visual comparison of the motion of our model-Hydra versus a video of real Hydra. In the next chapter, we discuss the results and analysis our model produced.

2.1 Bead-spring Model of Hydra

The computer model of Hydra is composed of beads of a unit mass connect by springs. Ten beads are arranged in the form of a circle of diameter D and connect via springs of stiffness κ_{ind} . Two such circular arrangements are connected together and form a cylindrical tube we call a "segment". 49 such segments are stacked on top of each other and connected again by Hookean springs to form a longer cylindrical tube, which we will use in our simulations as the model Hydra [17], [18], [19].

For the cylindrical tube to react correctly to different types of forces, there are several types of spring connections made within every segment. For example, opposite vertices (beads) were connected together to simulate internal structure; diagonally opposite vertices were connected to resist shear, etc.

The network of springs which have their own individual stiffness constant k_{ind} , also has an overall stiffness k_{eff} . The effective stiffness can be calculated by following some modifications of the usual parallel and series law of adding spring constants.

Since the model-Hydra has its stiffness in terms of spring constant, whereas the experimental values are in terms of Young's modulus, we need to establish a relation between the two so that we can put correct values in our simulations.

For a hollow cylindrical tube of length L and cross-sectional area A , we know that the stress (σ) versus strain (ϵ) equation has Young's modulus (Y) as

$$\sigma = Y\epsilon \quad (2.1)$$

Where

$$\epsilon = \frac{\Delta x}{L}; \sigma = \frac{F}{A} \quad (2.2)$$

Here F is the force exerted along its long axis. We also know that for a spring of length L and stiffness constant k , if we exert the same force F along its axis, we can write the Hooke's law as

$$F = -k\Delta x \quad (2.3)$$

If we substitute eq [2.2] into eq [2.1], and compare it with eq [2.3] we can extract the relationship between the Young's modulus and spring constant as

$$|k| = \frac{|Y|A}{L} \quad (2.4)$$

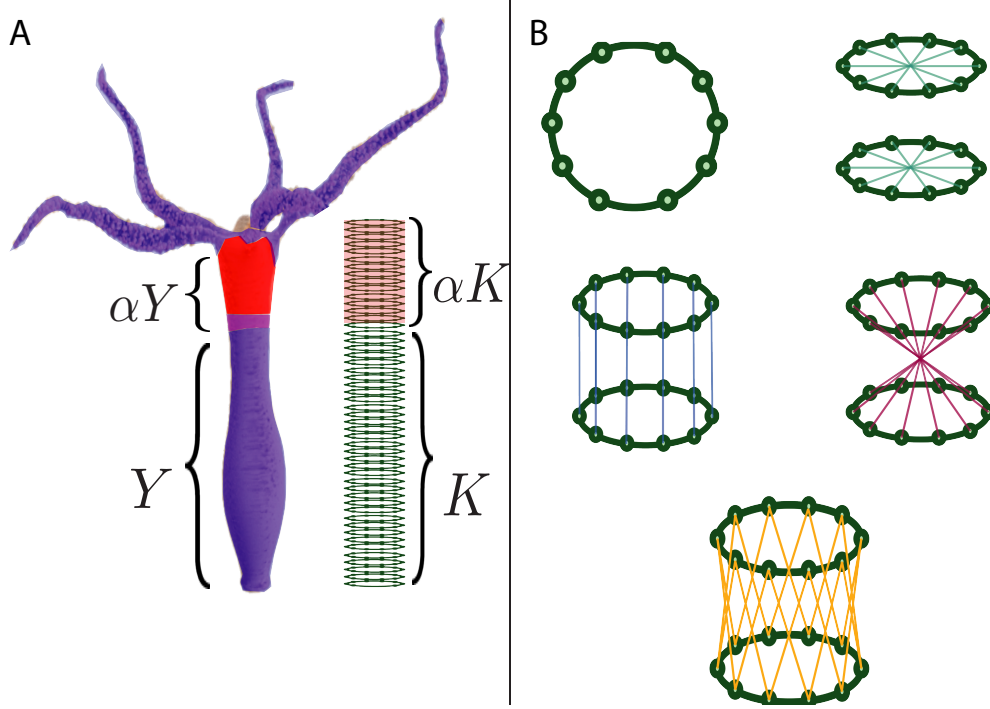


Figure 2.1: **A** Hydra's tubular body column is modelled by a network of beads connect with Hookean springs arranged in the form of a cylinder. The upper 25% of the model-Hydra has the effective stiffness value, which is α times the rest. Here α is an adjustable parameter, whose experimentally obtained value is 3. **B** cross-section view of the model-Hydra shows ten beads arranged circularly to form a ring. We made appropriate connections to produce appropriate responses to shear, torsion etc.

This k is the effective spring constant, resulting from the contribution of all the springs together. In the next section, we extract a relation between this effective stiffness constant (k_{eff}) and the stiffness of individual springs (k_{ind}), so that we can tune the individual stiffness and read off what the effective stiffness is.

2.2 Response to axial deformation of model-Hydra

Ideally, when we have two springs, with spring constants k_1 and k_2 connected in parallel, the resultant stiffness are additive, so the effective stiffness can

be written as,

$$k = k_1 + k_2 \approx f(k_1, k_2) \quad (2.5)$$

Similarly, when the springs are connected in a series we get

$$k = \left[\frac{1}{k_1} + \frac{1}{k_2} \right]^{-1} \approx f(k_1, k_2) \quad (2.6)$$

In both cases, the effective stiffness is function of individual stiffness of the springs, which is independent of the amount of deformation and is thus a constant with respect to Δx or strain in continuum case. In our model, not only do we have parallel and series connection which lead to a constant effective stiffness, we also have diagonally connected springs. (fig 2.2C) This results in a slightly more complicated effective stiffness, which has a strong dependence on the amount of strain.

$$k \approx f(k_1, k_2, \epsilon); \epsilon = \frac{\Delta x}{x_0} \quad (2.7)$$

However, this is closer to real world since the stiffness constant does indeed depend on the amount of strain we put in. The effective stiffness in our model-Hydra varies about 20% during the course of the simulation.

To find out the exact relation between the individual spring constants and the overall effect spring constant, we continuously deformed our model-Hydra along its long axis and plotted the effective spring constant versus the strain and versus the individual spring stiffness (fig 2.3). We can see in the figures that even at a high strain of 1, which is a non-linear regime, the effective stiffness by only about 20%. We can also see that for a fixed value of strain; the effective stiffness varies linearly with the stiffness of individual springs.

In all our simulations, for the sake of simplicity, all the k_{ind} are set to have the same value in the lower three-quarters of the Hydra body, say $k_{ind} = k_0$, whereas the upper 25% of the body column has the stiffness of $\alpha \times k_0$. As discussed in the previous sections, we will vary this α parameter to compare the cases of uniform stiffness $\alpha = 1$ and the experimentally obtained stiffness gradient where $\alpha \approx 3$.

2.3 Implementation of external forces

Hydra is a freshwater organism; thus its motion is subjected to various types of external forces, including drag due to water's viscosity, buoyancy, and

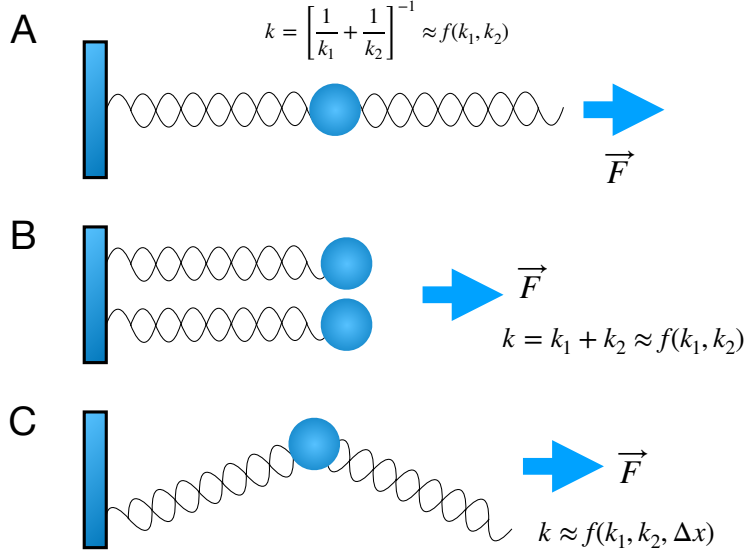


Figure 2.2: **A.** The effective spring constant follows the reciprocal addition law of spring constants when the springs are connected in series. **B.** Springs are connected in parallel leads to the individual stiffness being directly added together to get the effective stiffness. **C.** Model-Hydra, along with series and parallel connections, also has diagonal connections which results in a strong dependence of effective stiffness on the amount of strain.

gravity. In this section, we will discuss how these forces were incorporated. The exact numbers will be discussed in the last section.

Our model-Hydra is composed of 500 beads forming the cylindrical network. We calculate each type of force and distribute it evenly across all the beads. This implies that if force due to gravity is F_g , each bead is acted upon with a force of $F_g/500$, such that the overall force equals the total force.

Hydra's somersault motion lies in a low Reynolds number regime, thus we can approximate the drag force with a simple Stokes drag.

Based on the analysis of the videos, we can divide the motion of Hydra into two parts. The first part is the *contraction*, where the Hydra returns from its stretched position to its neutral length. This is followed by an upward motion, which straightens the bent part in the head region, leading to Hydra returning to its native, inverted state.

We know that the drag experienced by Hydra depends on its current geometry, the viscosity of water and its velocity. While this can become a relatively complex task, since the geometry of Hydra varies with time, we

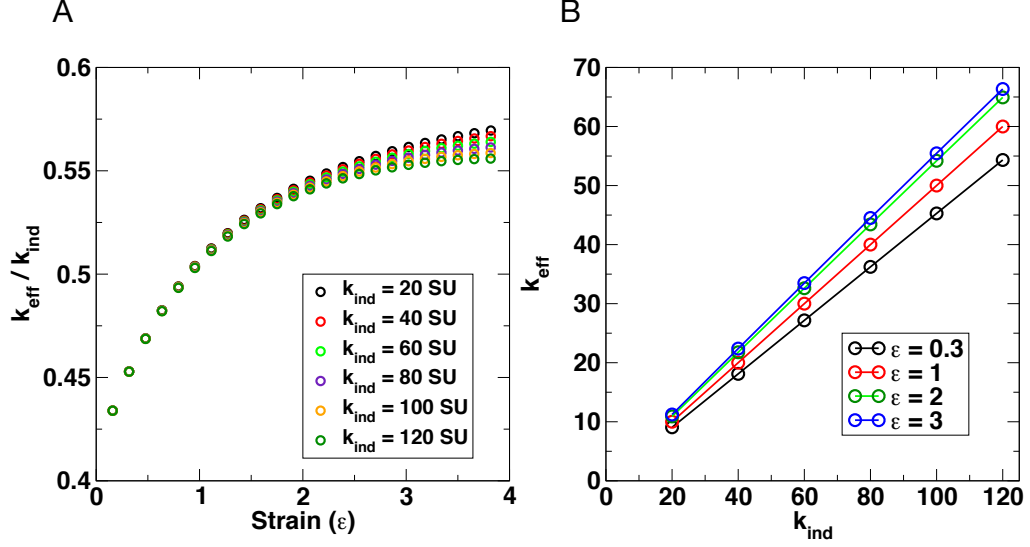


Figure 2.3: **A.** The effective stiffness (k_{eff}) variation (normalized by constant individual stiffness (k_{ind}) versus strain (ϵ). It can be seen that the effective stiffness of model-Hydra varies only about 20% during the course of the simulation, which occurs below $\epsilon = 1$. **B.** The effective stiffness (k_{eff}) varies linearly with the individual stiffness (k_{ind}) for any fixed strain.

can simplify the problem by comparing our model-Hydra with a cylindrical tube moving inside water along its longitudinal and transverse axis.

The contraction of model-Hydra experiences a drag very similar to a cylindrical tube moving inside water along its longitudinal axis, while the upward motion is similar to a cylinder moving transversely.

The drag constant experienced by a cylinder is well known([11],[20]), and it's given by the following equation,

$$\Gamma_{\perp} = \frac{4\pi\eta L}{\ln(L/D)}; \Gamma_{\parallel} = \frac{2\pi\eta L}{\ln(L/D)} \quad (2.8)$$

Here, L and D are length and diameter of the cylinder, while η is the water's viscosity (fig 2.4)

Since the difference between the two is not too much, for our simulations we have used the average of the two,

$$\Gamma_{sim} = \frac{\Gamma_{\perp} + \Gamma_{\parallel}}{2} \quad (2.9)$$

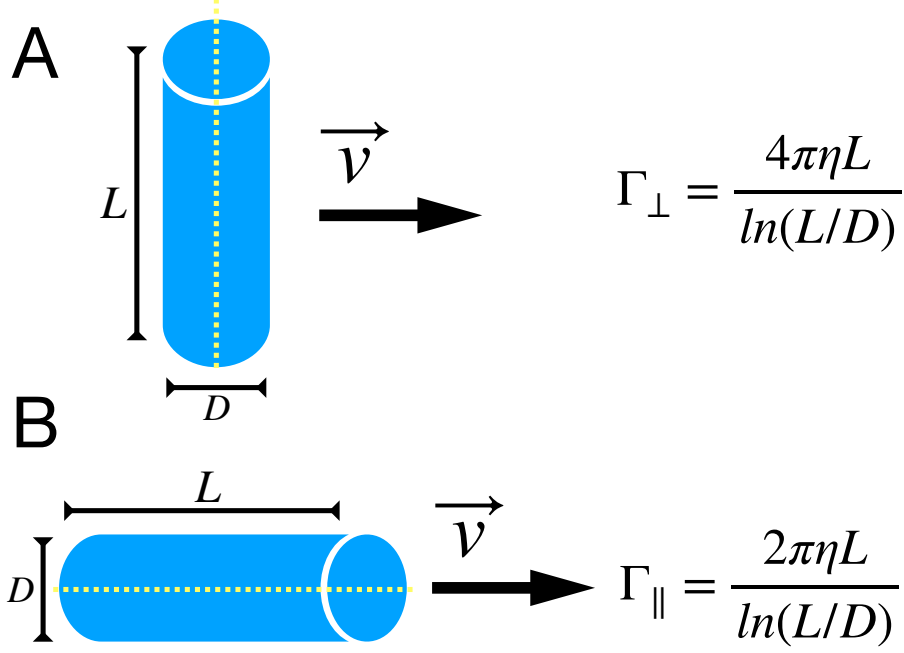


Figure 2.4: **A.** The drag experienced by a thin and long cylinder when it travels along its short axis in water. **B.** The drag experienced by a long thin cylinder when it travels along its long axis in a viscous medium. In **A** and **B**, η is the viscosity of the medium, while L and D are the length and diameter of the cylinder respectively.

As discussed in above, we implement this by giving each bead (mass-point) $1/500$ of this force, and we include this in the drag constant itself. So each bead has a drag constant associated with it given by $\Gamma_{bead} = \Gamma_{sim}/500$. Since Hydra is suspended in water, it experiences both an upward buoyant force, and a downward gravitational pull. We can say that Hydra experiences an effective gravitational force, which is a small fraction of the real gravitational force. Each bead in the simulations experiences $1^{th}/500$ of this effective gravitational force g_{eff} , where $g_{eff} = \beta g$, β being some fraction and $g = 9.8m/s^2$.

Apart from these external forces, we have also implemented a hard-sphere like repulsive force to simulate the substrate on which Hydra sticks itself. This repulsive force is present to make sure that Hydra does not cross through the surface upon which it performs its somersault.

This external repulsive force is modelled by a Lennard-Jones 6-12 potential [21], which is cutoff such that we only include its repulsive part. This is also known as the Weeks–Chandler–Anderson (WCA) potential [22]. It's obtained in the following way, we start with a regular LJ potential and take its derivative to get the force,

$$V_{LJ}(r) = 4\epsilon_{LJ} \left(\left[\frac{\sigma_{LJ}}{r_{LJ}} \right]^{12} - \left[\frac{\sigma_{LJ}}{r_{LJ}} \right]^6 \right) \quad (2.10)$$

$$F_{LJ}(r) = -\frac{\partial V_{LJ}(r)}{\partial r} = 48\epsilon_{LJ} \left(\left[\frac{\sigma_{LJ}^{12}}{r_{LJ}^{13}} \right] - \frac{1}{2} \left[\frac{\sigma_{LJ}^6}{r_{LJ}^7} \right] \right) \quad (2.11)$$

By equating $F_{LJ} = 0$, we can find the minima of V_{LJ} at $2^{1/6}\sigma$. We can thus tweak the force function by truncating it at this point, such that only the repulsive part remains. We do this by defining a new function which we use in the simulations,

$$F_{LJ}^* = \begin{cases} 48\epsilon_{LJ} \left(\left[\frac{\sigma_{LJ}^{12}}{r_{LJ}^{13}} \right] - \frac{1}{2} \left[\frac{\sigma_{LJ}^6}{r_{LJ}^7} \right] \right) - F_{LJ}(2^{1/6}\sigma); \forall r < r_c \\ 0; \forall r > r_c \end{cases} \quad (2.12)$$

In our simulations, this force acts as a repulsive force only in the vertically up direction, similar to a floor.

2.4 Time evolution of model-Hydra: Damped velocity verlet algorithm

Each bead in our simulation is evolved in time using a modified version of velocity verlet algorithm [23], [24], [25], [26]. The velocity verlet algorithm is typically used in molecular dynamics simulations however, its scale-independent and can be used in our simulations as well.

If we calculate the net combined force on a given bead (say i^{th}), the general expression for the time evolution of position and velocity, in velocity-verlet algorithm is given by

$$x_{n+1} = x_n + \Delta_t v_n + \frac{1}{2} \Delta_t^2 a_n; \quad (2.13)$$

$$v_{n+1} = v_n + \frac{1}{2} \Delta_t (a_{n+1} + a_n) \quad (2.14)$$

Where x_n, v_n, a_n are position, velocity and acceleration at the n^{th} step respectively.

This expression is derived on the assumption that the acceleration/force only depends on the position in the previous steps, and not on velocity. However, as we have discussed above, the damping term is velocity dependent and thus $a(x_n, t_n) \rightarrow a(x_n, v_n, t_n)$.

In our case the damping is linear, and the damping force $G(v)$ can be written as

$$G(v) = \gamma v = \frac{x_{n+1} - x_{n-1}}{2\Delta_t} + O(\Delta_t^2) \quad (2.15)$$

Using this, we can modify the velocity verlet algorithm to get the following expressions:

$$x_{n+1} = x_n + \Delta_t v_n + \frac{1}{2} \Delta_t^2 a_n \quad (2.16)$$

$$v_{n+1} = \frac{1}{1 + \Delta_t \gamma / 2m} [v_n(1 - \Delta_t \gamma / 2m) + \frac{\Delta_t}{2m} (F_{n-1} + F_n)] \quad (2.17)$$

Refer to Appendix [B](#) for further details about this derivation.

2.5 Visual comparison of model-Hydra with real Hydra videos

Before attempting to compare our simulations at a quantitative level with the real world, we compared the output of our simulations with videos of real Hydra qualitatively to see if our simulations display similar characteristics.

One such characteristic, which is the focus of this study, is that our simulations must follow a similar two-part process of 1. contraction and 2. standing upright by straightening the bent part.

Our simulations start by fixing both ends of the model-Hydra in a stretched position. The shoulder region makes an angle of 45 with the substrate since the rest of the motion is not passive. We observed in the videos of real Hydra polyps, that the once the Hydra is in its upright position, it makes a slight angle with the substrate, which is subsequently fixed extending one of its tentacles and pulling itself in a vertical position.

Looking at a side by side comparison of the simulations versus the real Hydra (fig [2.5](#)), we can see that the simulations indeed show a similar type of two-part motion.

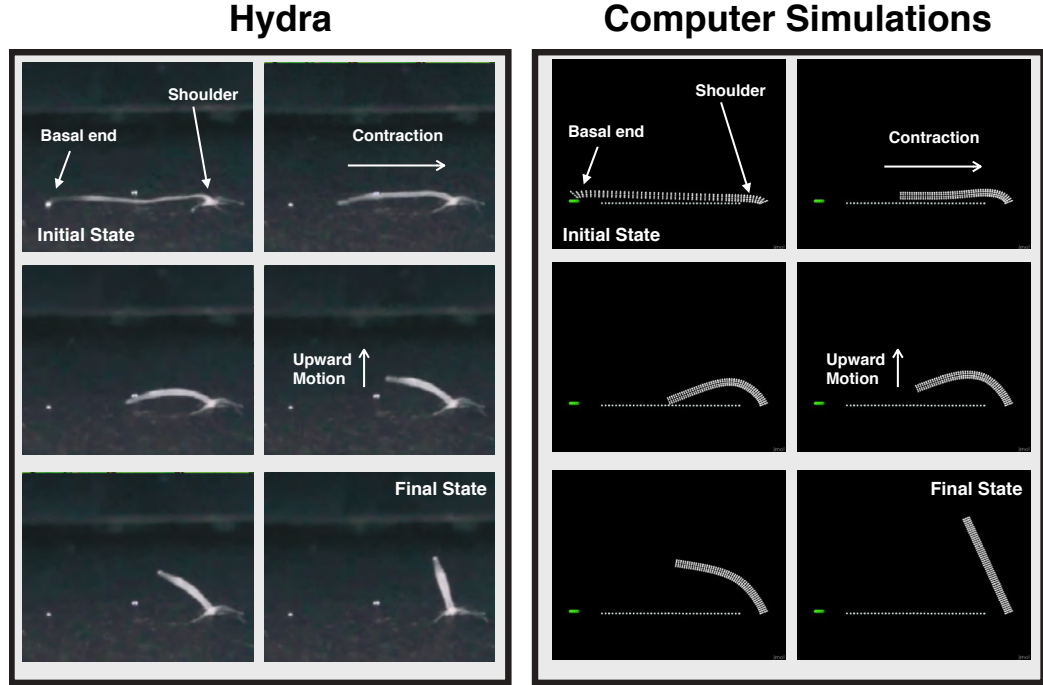


Figure 2.5: **A.** Real images of the two part motion of Hydra polyp, extracted from the frame by frame video analysis of Hydra motion. **B.** Snapshots from the simulations. Both **A** and **B** show a contractile motion, followed by an upward motion. Model-Hydra in the simulations is initialised with a strain of $\epsilon = 0.8$

2.6 Simulation units

As discussed in the introduction, we have put the absolute minimum set of parameters to understand the role of stiffness gradient. Further refinement and introduction of more parameters in the model will only be needed if the phenomenon cannot be explained by these parameters.

A stretched Hydra simulation can be characterised by the following parameters

1. Young's modulus: Y
2. Length: L
3. Cross-sectional area: A

4. Energy stored: E

5. Mass: M

6. Drag: Γ

In order to match the real world with the simulations, we need a dimensionless quantity that can translate the units used in the real world into simulations units and vice-versa.

Taking the parameters mentioned above, we can construct such a parameter ξ , which can be written as

$$\xi = \frac{\Gamma L^{3/2}}{E} \sqrt{\frac{YA}{M}} \quad (2.18)$$

We have already established a simple relation between the Young's modulus and spring constant in the previous sections. If we utilize that relation here and substitute for $Y \rightarrow kL/A$, we get

$$\xi = \frac{\Gamma L^2}{E} \sqrt{\frac{k}{M}} \quad (2.19)$$

Following is a tabulated approximate data about Hydra available from the experiments (table 2.1) To get the value of dimensionless parameter ξ , we

Mass M	$10^{-7}kg$
Length L	$5 \times 10^{-4}m$
Diameter D	10^4m
Water's viscosity η	$10^{-3}Pa$

Table 2.1: List of approximate experimentally observed data for Hydra polyps

start by estimating all its dependent variables

1. Elastic Energy (E): To get a rough estimate of the stored elastic energy in Hydra, we take the experimentally measured Young's modulus value to be around $1000Pa$. We also assume a linear stress-strain curve i.e. $\sigma = Y\epsilon$. The stored elastic energy per unit volume is given by the integral of this stress-strain curve. For the sake of simplicity, we assume that the Hydra stretches itself to twice its length, which means that the strain $\epsilon = 1$. Thus we can write

$$E/V = \int_0^1 \sigma d\epsilon \implies E = V \int_0^1 Y\epsilon d\epsilon = \frac{YV\epsilon^2}{2} \Big|_0^1 = \frac{YV}{2} \quad (2.20)$$

Using the values of inner and outer radii for the Hydra and its length from table 2.1 we get the stored elastic energy value to be

$$E = \frac{YV}{2} = \frac{10^3 Pa \times \pi(1^2 - 0.05^2) \times 10^{-8} m^2 \times 5 \times 10^{-3}}{2} \approx 6 \times 10^{-8} J \quad (2.21)$$

2. Stoke's drag coefficient for Cylinder Γ : The amount of drag experienced by Hydra is determined by its Stoke's coefficient. As discussed in the previous sections, Hydra motion occurs in a low Reynolds's number condition, and thus the drag force is linearly dependent on the velocity. The diameter to length ratio D/L for the Hydra body is a small fraction, and it can be approximated as a long, thin cylindrical tube ([11] and [20]). The drag coefficient in this approximation is divided into two parts, one parallel to the cylinder axis (running along its length), which we call Γ_{\parallel} and the other perpendicular to the axis, Γ_{\perp} . Ideally, Γ_{\parallel} should be used during the contraction and Γ_{\perp} during the upward motion ,however due to these being very close to each other, we can take their average and get

$$\Gamma = \frac{\Gamma_{\parallel} + \Gamma_{\perp}}{2} = \frac{3\pi\eta L}{\ln(L/D)} \approx 1.2 \times 10^{-5} Ns/m \quad (2.22)$$

3. Mass (M): A rough estimate of Hydra's mass can be made by observing the fact that the density of Hydra should be very close to that of water. Therefore the mass can be calculated as

$$M \approx \pi \times (r_{outer}^2 - r_{inner}^2) \times \rho_{H_2O} = 10^{-7} kg \quad (2.23)$$

4. Stiffness constant of equivalent spring (k_{eff}): We use the previously calculated relation between the Young's modulus and the spring constant to calculate the stiffness of an equivalent spring by using the same average value of Young's modulus (1000 Pa) and cross-sectional area of Hydra

$$k_{eff} = \frac{YA}{L} = \frac{10^3 Pa \times \pi \times (r_{outer}^2 - r_{inner}^2)}{L} \approx 0.5 \times 10^{-2} N/m \quad (2.24)$$

Using these, we can estimate ξ as

$$\xi = \frac{\Gamma L^2}{E} \sqrt{\frac{k}{M}} = \frac{(1.2 \times 10^{-5} Pa)(5 \times 10^{-3} m)^2}{6 \times 10^{-8} J} \sqrt{\frac{0.5 \times 10^{-2} N/m}{10^{-7} kg}} \approx 1.1 \quad (2.25)$$

The simulation parameters are selected, such that this dimensionless quantity remains unchanged in the simulation units. Choosing the stiffness

constant fixes the stored elastic energy of the system. Using the effective stiffness value of $20su$, where su stands for simulation units, the stored energy can be calculated as $1/2k_{eff}\Delta x_{sim}^2$. The neutral length of the simulation Hydra being $30su$, upon being stretched twice its length, gives the value of $\Delta x_{sim} = 30su$. Using these values along with the simulation mass as $500su$ (each bead being assigned a mass of 1 unit, with 500 beads forming the cylinder), we get

$$\xi_{sim} = \frac{\Gamma_{sim}L_{sim}^2}{E_{sim}}\sqrt{\frac{k_{sim}^{eff}}{M_{sim}}} = 0.02\Gamma \quad (2.26)$$

Since ξ_{sim} must be equal to ξ , means that

$$\eta_{sim} = 0.02\Gamma = \eta = 1.1 \quad (2.27)$$

$$\implies \Gamma_{sim} \approx 55su \quad (2.28)$$

Since our model-Hydra consists of 500 beads, each bead can be assigned a viscous drag coefficient of $\Gamma_{sim}^i = \Gamma_{sim}/500 \approx 0.11su$

Estimation of Time Units

We can construct a unit of time using the drag coefficient, Γ , neutral length of the Hydra, and the elastic energy stored for a strain of $\epsilon = 1$.

$$\tau = \frac{\Gamma L^2}{E} \quad (2.29)$$

Since these quantities have already been fixed in the units section, the calculated time in the simulation units must correspond to the time calculated using the same formula in SI units. Therefore,

$$\tau_{sim} = \frac{\Gamma_{sim}L_{sim}^2}{E_{sim}} = \frac{55 \times 30^2}{9000} = 5.5su \quad (2.30)$$

This must be equal to

$$\tau = \frac{\Gamma L^2}{E} = \frac{1.2 \times 10^{-5}Ns/m \times (5 \times 10^{-3})^2m}{6 \times 10^{-8}} = 5 \times 10^{-3} \quad (2.31)$$

Comparing the two, we get the relation between SI units and simulation units as

$$1s = 1.1 \times 10^3su \quad (2.32)$$

It could be argued that there are several other ways to combine the existing parameters to define the simulation time, for example, a time unit could also be defined by combining the effective stiffness of the equivalent spring and the mass of Hydra as $\tau^* \sim \sqrt{m/k}$.

However, this method of defining time does not capture the parameters of the environment in which the Hydra resides, namely, the viscous drag. On a qualitative basis, it can be argued that had the time in the simulation been defined as τ^* , the simulation would not have been uniquely governed by τ^* as we changed the viscosity.

On a more quantitative level, we compared the time evolution of model-Hydra for three different values of stored elastic energy and viscous drag, such that the ratio of the drag with the energy is the same.

We can see in the figure (ref [2.6](#)) that despite having three different values of drag and energies, all three curves of time evolution of model-Hydra collapse on top of each other. This proves that our selection of τ parameter is justified.

We can, therefore, summarize the correspondence between the units used in our simulations and the SI units used in experiments in table [2.2](#)

Dimension	Simulation Units	SI Units
Length [L]	1	$0.17 \times 10^{-3}m$
Mass [M]	1	$2 \times 10^{-7}kg$
Time [T]	1	$0.91 \times 10^{-3}s$

Table 2.2: Table summarizes the correspondence between the simulation units and the SI units used in experiments

2.7 Initial setup and objective of the simulations

Having fixed all the parameters and qualitatively validated the model, we can begin to analyse the model. To understand why Hydra developed an elasticity gradient, we left a free parameter α in the simulations. When $\alpha = 1$, the model-Hydra has a uniform stiffness throughout its body column, while when $\alpha = 3$, the stiffness gradient is similar to that of the experiment.

Since the model-Hydra could have any value of stiffness gradient, we can also perform simulations for several different values of α , and test if there is any unique advantage of having an $\alpha = 3$ variation.

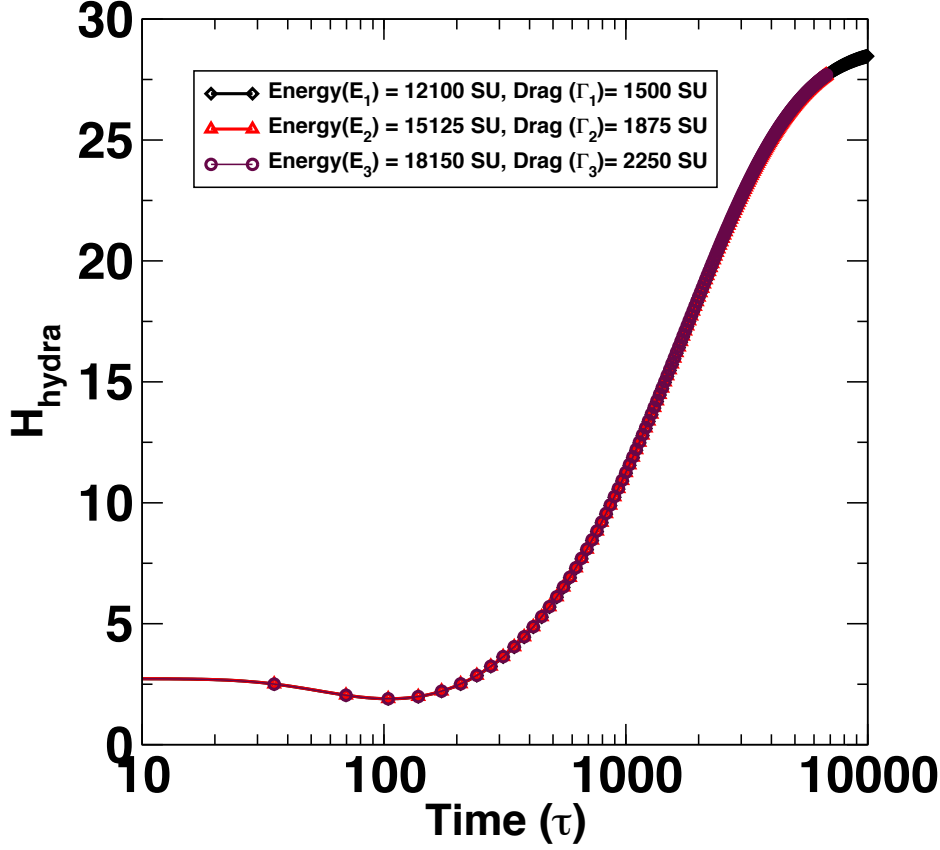


Figure 2.6: Model-Hydra is released from its basal end and the centre of mass position of its basal end is tracked with time. The figure shows the height of the centre of mass (average position of the 10 beads in the basal end) from the substrate to which the model-Hydra is attached. For three different values of drag coefficient (Γ_1, Γ_2 and Γ_3) paired with three different values of energy (E_1, E_2 and E_3) such that $\Gamma_1/E_1 = \Gamma_2/E_2 = \Gamma_3/E_3$, all three curves overlap each other, which shows that $\tau = \Gamma L^2/E$ uniquely determines the time evolution of Hydra. This simulation is conducted at the strain of $\epsilon = 0.2$, however, this remains true for any value of ϵ .

If we see any clear advantage with $\alpha = 3$ case, we would like to explain the reason behind the same by comparing several different quantities like

momentum, kinetic and potential energy, etc between $\alpha = 3$ and other values of α .

Our simulations have been conducted with two different initial stretched positions of Hydra, one with a small strain of $\epsilon = 0.2$, while the other being a larger strain of $\epsilon = 0.8$. A strain much larger than this is not only out of the scope of our simulations, but it is also not generally seen in real Hydra polyps.

Chapter 3

Simulation results and discussion

All our simulations are performed in two different cases, one where the gravity and buoyancy forces are turned on, while the other where they are switched off.

Both these cases are required to develop an understanding of Hydra's motion, as each case achieves a particular objective.

1. With Gravity and Buoyancy turned off, we want to explore the internal dynamics of model-Hydra as it evolves in time. We want to probe if there is a clear advantage, in terms of efficiency, for a Hydra with a gradient.
2. If we establish some kind of clear advantage of having a stiffness gradient, we wish to ask if this advantage becomes the deciding factor in terms of Hydra's ability to rise when the external forces of Gravity and Buoyancy are turned on.

In the next sections, we compare and contrast multiple different model-Hydras by looking at different quantities.

It needs to be noted that for our comparisons to have an equal footing, for all the model-Hydra cases from $\alpha = 1$ to $\alpha = 30$, the absolute values of Young's modulus has been selected such that the total energy stored for a given strain (ϵ) remains the same. This means that the case where model-Hydra has a uniform stiffness ($\alpha = 1$) and the model-Hydra with any gradient ($\alpha > 1$) have the same energy. This is a major distinction between our simulation and the experiments, where the real Hydra's gradient was destroyed such that the entire polyp has the lower Young's modulus value of $500Pa$.

3.1 Basal tip height versus time plots and Relaxation time

We begin our simulations by initially quantifying the centre of mass position of the basal tip of model-Hydra, as it evolves in time. Our model-Hydra starts from its head region fixed at one end, while the other end (basal) is stretched and fixed at a small strain of $\epsilon = 0.2$. (fig 3.1)

The centre of mass position of the basal tip is calculated by averaging the positions of the ten beads, which form the circular tip of model-Hydra. We call the vertical movement as Hydra as H_{Hydra} while the movement along the direction of its contractile motion (along its long axis) is termed as L_{Hydra} .

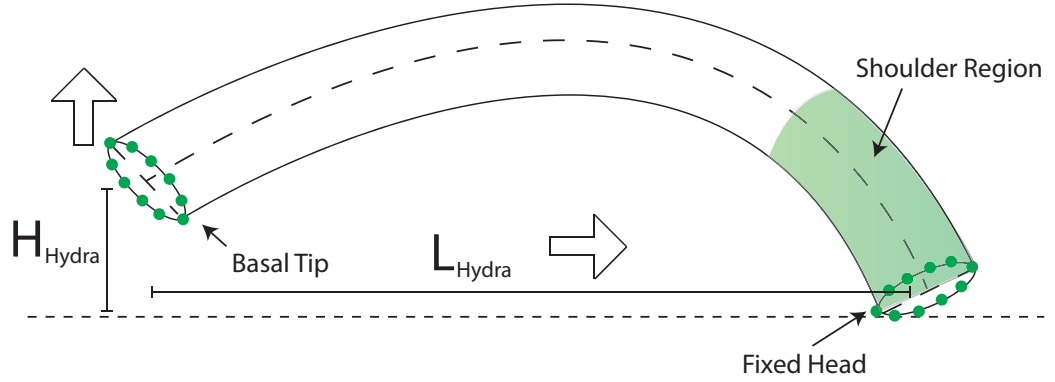


Figure 3.1: Schematic of the simulations shows the basal-tip and the shoulder-base composed of circularly arranged beads. Beads are not shown on the body surface for clarity. The height of the centre of mass of the basal-tip is labelled as H_{Hydra} , whereas the movement along the horizontal direction is labelled by the L_{Hydra} coordinate. The region shaded in green is the first 25% of Hydra's body. It has a higher observed stiffness value than the rest of the body column.

After the initial contraction is complete, the model-Hydra starts with an upward motion. The basal-tip's behaviour during this upward motion can be understood better by comparing it with a sphere with some initial velocity (\vec{v}), moving in the same vertical direction in a viscous medium. For such a sphere, a differential equation can be written as

$$\frac{d^2 z(t)}{dt^2} + \frac{\Gamma}{m} \frac{dz(t)}{dt} = 0 \quad (3.1)$$

Upon solving this equation, we get the functional form of $z(t) \sim (1 - e^{t/\tau})$. To account for some deviations from this behaviour, we write the equation

for the upward motion of basal tip with two free parameters a and b , such that $z(t) = a(1 - e^{t/\tau}) + b$. Both $H_{Hydra}(t)$ (fig 3.2 A) and $L_{Hydra}(t)$ (fig 3.2

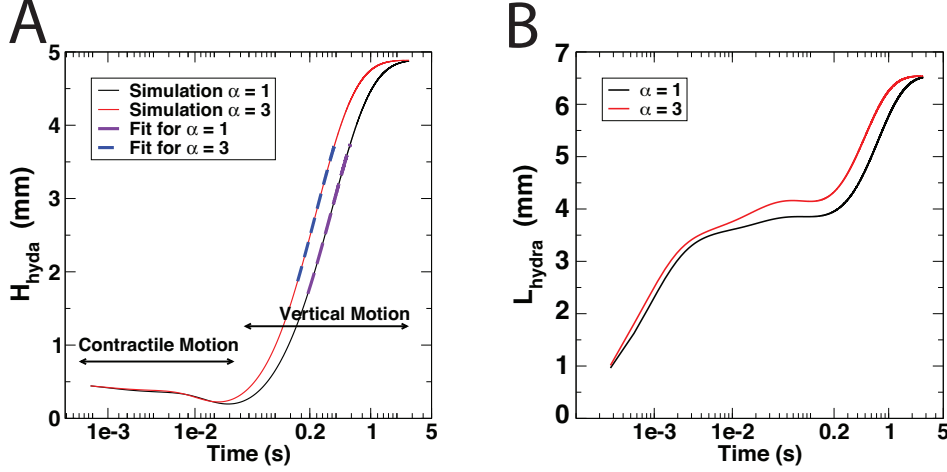


Figure 3.2: **A.** The vertical (H_{Hydra}) and **B.** the horizontal (L_{Hydra}) position of the basal-tip of model-Hydra is plotted with time for $\alpha = 1$ (uniform) and $\alpha = 3$ (gradient) cases. Both these cases are plotted for a small strain of $\epsilon = 0.2$. The plots for $\epsilon = 0.8$ show similar behaviour.

B) are plotted on a semi-logarithmic scale, to see if the upward motion does indeed have an exponential nature. It can be seen in the plots that during the upward motion, the $H_{Hydra}(t)$ versus t does become straight, which is a signature of an exponential nature. We fit each of these $H_{Hydra}(t)$ plots with the above calculated function $z(t) = a(1 - e^{t/\tau}) + b$, to extract τ , which we call the "relaxation time". This relaxation time is proportional to the time taken by the model-Hydra to complete its motion.

We repeated the simulations for multiple values of α , ranging from $\alpha = 1$ which is the uniform stiffness, to $\alpha = 30$. For each such simulation, we plotted the $H_{Hydra}(t)$.vs. t curve and extracted τ by fitting the plots with $z(t)$. We carried out this analysis for both large $\epsilon = 0.8$ and small $\epsilon = 0.2$ values of strains.

We define Power P as the initial potential energy of model-Hydra, divided by this τ , or $P = E_{tot}/\tau$. The extracted τ can be treated as a function of α , which carries over to the definition of Power as well, so $P \rightarrow P(\alpha) = E_{tot}/\tau(\alpha)$.

We plotted $P(\alpha)$ versus α for the two strain cases (fig 3.3).

We can see from fig 3.3 that in both $\epsilon = 0.2, 0.8$ cases, a clear advantage in terms of Power is seen for the model-Hydra with an elasticity gradient.

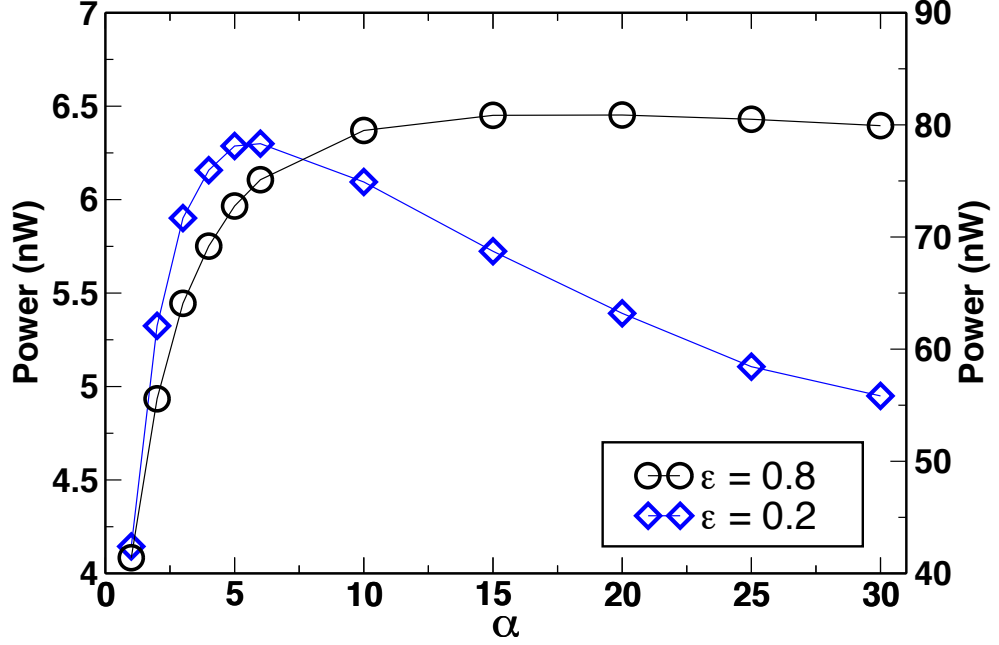


Figure 3.3: Power $P(\alpha)$, defined as the initial total stored potential energy E_{tot} divided by the relaxation time $\tau(\alpha)$ is plotted for small $\epsilon = 0.2$ and large $\epsilon = 0.8$ values of strains. The initial stored potential energy intentionally kept to be independent of the values of α , and only depends on the initial strain.

It is interesting to note that despite all the α having the same initial energy (for a given ϵ), the $\alpha = 3$ model-Hydra is significantly more powerful in its somersault motion.

We can also see that there is a significant jump in the Power advantage as we go from $\alpha = 1 \rightarrow \alpha = 2$ and from $\alpha = 2 \rightarrow \alpha = 3$. However, the significance of the Power gain diminishes sharply beyond $\alpha = 3$. In particular, $\alpha = 1 \rightarrow \alpha = 3$ shows a gain in Power by 45% – 50%, while going from $\alpha = 3 \rightarrow \alpha = 6$ shows only about 8% – 10% further advantage.

Fig 3.3 also shows peak and a plateau for $\epsilon = 0.2$ and $\epsilon = 0.8$ cases respectively. These can be explained by the fact that given all model-Hydras have been kept at the same initial energies, to achieve a stiffer shoulder region, we must decrease the stiffness of the basal region. Beyond a certain α , the basal region starts to become floppy and is unable to hold itself together well

enough to resist the viscous drag. This tipping point occurs at around $\alpha = 5$, which is close to the experimental value of $\alpha = 3$.

It can be speculated that Hydras had a significant advantage in terms of Power to resist the viscous drag by developing a sharp gradient along their body column. They settled at a stiffness ratio of $\alpha = 3$ because 1. there was little to no advantage beyond this point (8% – 10% compared to initial 45% – 50%), and 2. Beyond about $\alpha = 5$, any advantage gained starts to become a disadvantage.

3.2 Total Potential and Kinetic energy with time

To further investigate our models, we plotted the total potential energy and the total kinetic energy of Hydra in both the uniform and the gradient ($\alpha = 3$) cases (fig 3.4). We observed that while a rapid dissipation of energy is seen in both cases, the $\alpha = 3$ case has a slower reduction of the potential energy. This can be attributed to the fact that there is a more efficient transfer of energy between the basal and the shoulder region, which leads to more energy saved in the stiffer segment to be utilized later during the upward motion. The uniform ($\alpha = 1$) model-Hydra can be seen to lose more of its potential energy during the initial contraction, potentially leading to an energy deficit during the upward motion. We see in the later sections when we switch on the gravity that this is indeed true.

3.3 Energy and Momentum of basal and shoulder region

In the last section, we discussed the advantage a stiffness gradient provides in terms of the Power and energy storage. However, our simulations showed that all model-Hydras, irrespective of the value of α , were able to pull themselves in an inverted position. This was not seen in the experiments, which showed that the Hydra with uniform stiffness was unable to stand inverted.

In this section and the sections which follow, we assume model-Hydra to have a density, which is 6% higher than water. Taking this density difference into account, we put in the appropriate gravitational and buoyant forces. This was done in accordance with the experimental results of the measurement of Hydra density, as discussed in chapter 1.

Interestingly, it was observed that model-Hydra with a uniform stiffness is unable to stand inverted, while model-Hydras with values of $\alpha > 1$ were able to. This was consistent with the experiments.

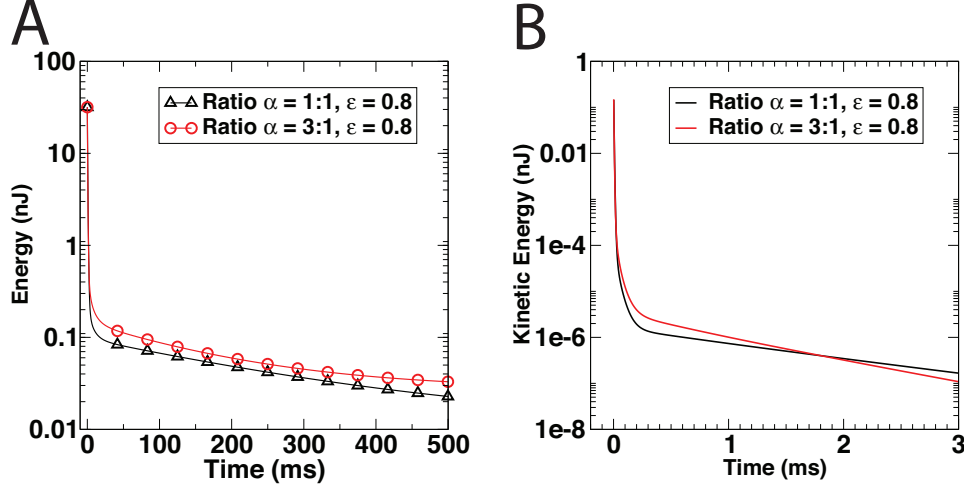


Figure 3.4: **A.** The total potential energy of model-Hydra is plotted with time. Hydra with $\alpha = 3$ has a much larger stored potential energy than the Hydra with $\alpha = 1$ at the end of its contraction, which occurs at about 100 ms. **B.** Total kinetic energy for the $\alpha = 3$ shows a similar behaviour, with a slower initial dissipation compared to uniform, but reverses later on.

In fig 3.5 - A, we can see that at time $t = 0$, just before the release of the ring at the basal end, the total potential energy (green) of the stretched model Hydra is the same for both $\alpha = 3$ and $\alpha = 1$. After release, the total energy decreases with time during the contractile motion due to viscous dissipation.

The energy stored only in the shoulder region (black) at time $t = 0$ is more for $\alpha = 1$ compared to $\alpha = 3$. After release the energy in the shoulder region decreases for both cases but remarkably at $t \sim 15ms$, the energy stored in the shoulder region of $\alpha = 3$ becomes greater than $\alpha = 1$. Since the retained potential energy till the end of contractile motion is more for $\alpha = 3$, this clearly indicates a more effective energy transfer from stretch to the bend for $\alpha = 3$. The energies stored in the shoulder region, the basal region, and the total energy are shown for a longer time to follow the energy behavior as the model Hydra goes from a contractile to an upward motion. At longer times (3.5-B), for $\alpha = 3$, the energy in the shoulder region remains greater than the energy stored in shoulder region for $\alpha = 1$. The minima at $t = 50ms$ (before the end of contraction) in basal stored energy for both $\alpha = 1$ and $\alpha = 3$ is due to small transfer from shoulder to basal region.

To understand the crossover of stored energies in the shoulder region seen in 3.5-A at $t = 15ms$, we plot the center of mass of velocities in x- direction of the basal and the shoulder region for both $\alpha = 1$ and $\alpha = 3$ cases. The

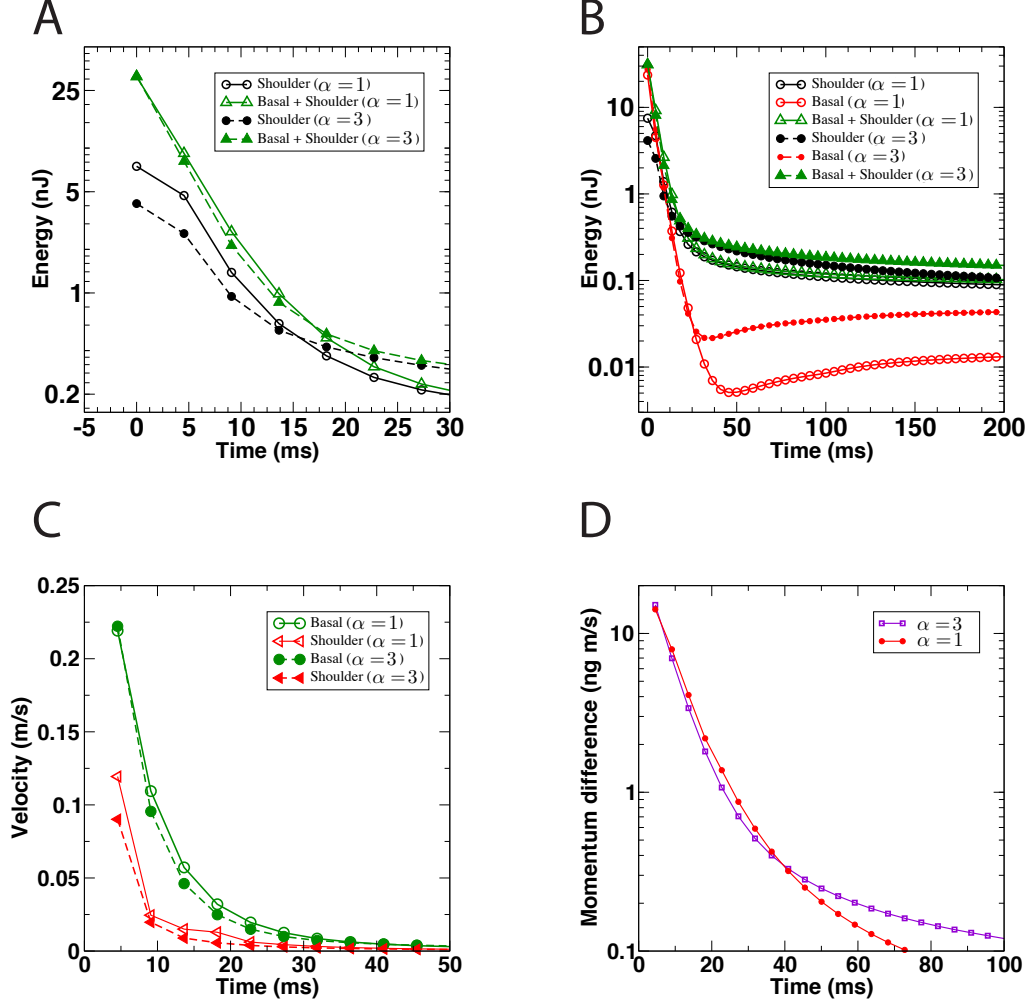


Figure 3.5: **A.** and **B.** Show the energy stored in basal and the shoulder region of Hydra as it evolves in time in the presence of gravity. **C.** The velocity of centre of mass of the basal and the shoulder region in both $\alpha = 1$ and $\alpha = 3$ cases. **D.** The difference in centre of mass momentum of the basal and the shoulder region of model-Hydra. A sharp crossover can be seen at time $t = 40ms$.

difference in velocities of the two regions allows the momentum transfer to produce a force on the shoulder region in positive x - direction. Presumably, this force is responsible for bending the shoulder.

The difference in momentum between the basal and the shoulder region is plotted as a function of time for both cases. Force exerted by the basal region on the shoulder is indicated by the slope at each point of the plot. The initial

($t < 30ms$) slope for $\alpha = 3$ case is steeper than the $\alpha = 1$. This indicates a larger force exerted by the basal region on the shoulder for $\alpha = 3$. The $\alpha = 3$ case has a larger momentum difference after contractile movement.

3.4 Average force at the junction

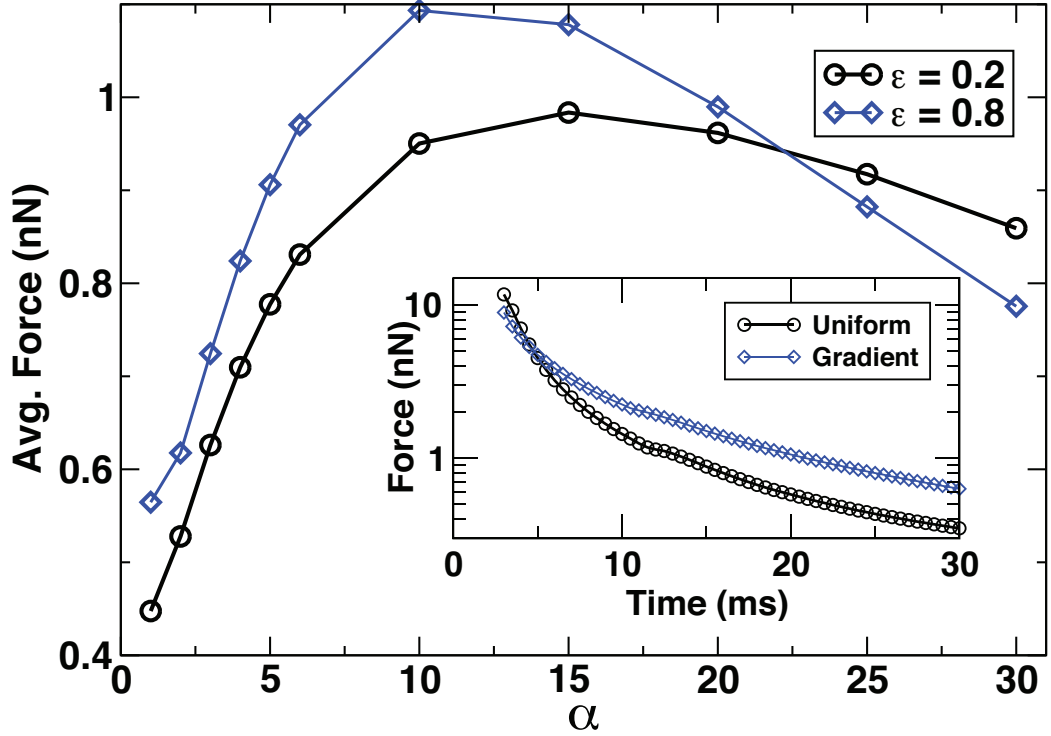


Figure 3.6: Force at the junction of basal and shoulder region averaged near the end of the contraction, is plotted as a function of stiffness gradient ratio α . Despite the same initial stored energy, the force at the junction for $\alpha = 3$ is about 50% greater than $\alpha = 1$. The inset shows the instantaneous force versus time for $\alpha = 1$ and $\alpha = 3$ case. It can be seen that the initial force is the same, but $\alpha = 3$ force remains larger as the model-Hydra evolves in time.

By analysing the energy and momentum plots in the previous section, we can safely assume that not only is the stiffness gradient responsible for a more powerful Hydra motion, but it also increases the efficiency of energy transfer between the basal and the shoulder region. This argument was supported further by plotting the average force at the basal and shoulder junction.

In fig 3.6 we plotted the force, which is averaged on a short time period of 50ms before and after the contraction, versus α . We observed that this force is significantly ($\approx 50\%$) larger for $\alpha = 3$ cases than $\alpha = 1$.

This larger force at the junction pushes the stiffer segment more than $\alpha = 1$, which leads to larger energy being stored in the shoulder region. It is this energy which is then efficiently utilized in helping the Hydra stand inverted.

fig 3.6 also shows a similar behaviour as fig 3.3, where going beyond a certain α value, the curve starts to turn around, and any advantage gained beyond this point becomes a disadvantage. In the case of fig 3.6 this tipping point or maxima occurs at a higher α of around $\alpha = 10 - 15$.

3.5 Estimation of the Threshold Energy ($E_{Threshold}$)

In the last sections, it was observed that the model-Hydra which can store energy more efficiently in the stiffer shoulder region, could complete the motion. We also concluded that its the energy stored in the shoulder region, which is responsible to turn the Hydra into its final inverted position. In this section we attempt to quantify, what is the minimum energy required by the shoulder region for the Hydra to stand inverted.

To carry out this calculation, we start by focusing on a single bead i . This bead will have to resist both the viscous forces and the damping forces during the course of the simulations.

To get the total energy dissipated, we have to integrate the viscous force faced by the bead over the entire time period of the simulations. The integration excludes the initial contraction time since we only care about the energy in the shoulder region. We define the time at the end of the contraction as t_c , and the time when the motion is completed as t_f , while the integration path is defined as $s_i(t)$. We can therefore write,

$$E_i^{Drag} = \int_{t_c}^{t_f} \Gamma v_i(t) ds_i(t) \quad (3.2)$$

To get the total energy needed we also need to add to this the gravitational potential energy of the bead at t_f , so

$$E_i^{Threshold} = \int_{t_c}^{t_f} \Gamma v_i(t) ds_i(t) + m_i g' h(t_f) \quad (3.3)$$

It is to be noted that we use an effective gravity g' instead of usual g , to account for the buoyant forces in water. Taking the sum over all 500 beads

gives us the threshold energy as

$$E_{Threshold} = \sum_{i=1}^{500} \left[\int_{t_c}^{t_f} \Gamma v_i(t) ds_i(t) + m_i g' h(t_f) \right] \quad (3.4)$$

This formula can easily be evaluated in the simulations. $E_{Threshold}$ is similar to a potential barrier, which the model-Hydra most cross in order to complete its motion.

3.6 Stored energy in the shoulder after contraction $E_{shoulder}$ versus time (t)

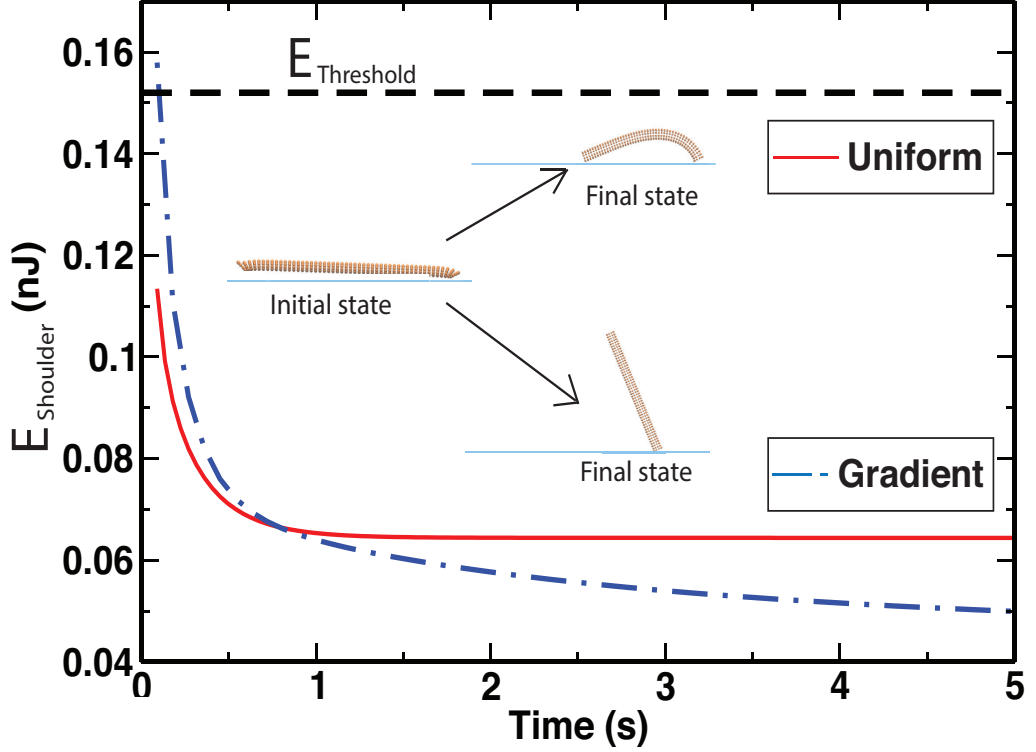


Figure 3.7: The energy in the shoulder region at the end of the contraction $E_{shoulder}$ is plotted with time for uniform ($\alpha = 1$) and gradient ($\alpha = 3$) cases. Only $\epsilon = 0.8$ case is shown, refer to appendix [C](#) for other cases.

To compare the calculated threshold energy with the $\alpha = 1$ and $\alpha = 3$ cases, we plotted the energy in the shoulder region at the end of the contraction for uniform and gradient cases. We can see in the plot that $\alpha = 3$ has an

initial energy larger than the threshold, while the uniform cases starts with a lower energy. The dashed solid line represents the calculated $E_{Threshold}$ as discussed in the last section.

As both model-Hydras evolve in time, we can see that $\alpha = 1$ curve becomes flat and is unable to use its leftover energy, while $\alpha = 3$ is able to use the shoulder energy to stand inverted effectively. As we discussed in the last section, starting with larger energy in the shoulder region ($E_{Shoulder} > E_{Threshold}$), which results from a more significant push/force at the junction during contraction, helps the Hydra in completing its motion.

3.7 Density difference ($\Delta\rho$) versus α : Phase Plots

The downward force on Hydra body column while trying to stand inverted is due to density difference ($\Delta\rho$) in Hydra tissue and water. The efficiency of energy transfer to work against this is large for greater stiffness variation (larger α). We have performed simulation runs for different parameters, and we plot a phase diagram of $\Delta\rho$ and α to find out criticality for standing inverted.

The simulations clearly show that the variation in tissue stiffness, characterized by α , facilitates efficient energy transfer from a stretch to a bend, which is used to overcome the downward force on the body column due to Hydra's higher density compared to that of water. Since this energy is used for overcoming the hydrodynamic drag and the weight of body column due to the density difference, the successful completion of somersault depends on two parameters specific to Hydra: $\Delta\rho$ and α .

Since experimentally observed Young's modulus is over-estimated owing to the treatment with Glutaraldehyde, we generated phase diagrams $\Delta\rho$ versus α for different values of Young's modulus. We observed that for extremely labile bodies ($Y < 10$ Pa), the energy stored in the stretch and transferred to the bend is lower than the threshold, and Hydra is unable to rise for all values of α .

On the other hand, for extremely stiff bodies ($Y > 10$ kPa), the energy required to stretch to 80% strain is large, and the transferred energy is always above the threshold such that Hydra is always able to rise for all values of α . These two extremes are far from the experimentally observed stiffness and its variation in real Hydra tissue.

Figure 4D depicts the phase diagram of $\Delta\rho$ and α at the experimentally observed values of Y . Note that to keep the amount of energy and strain

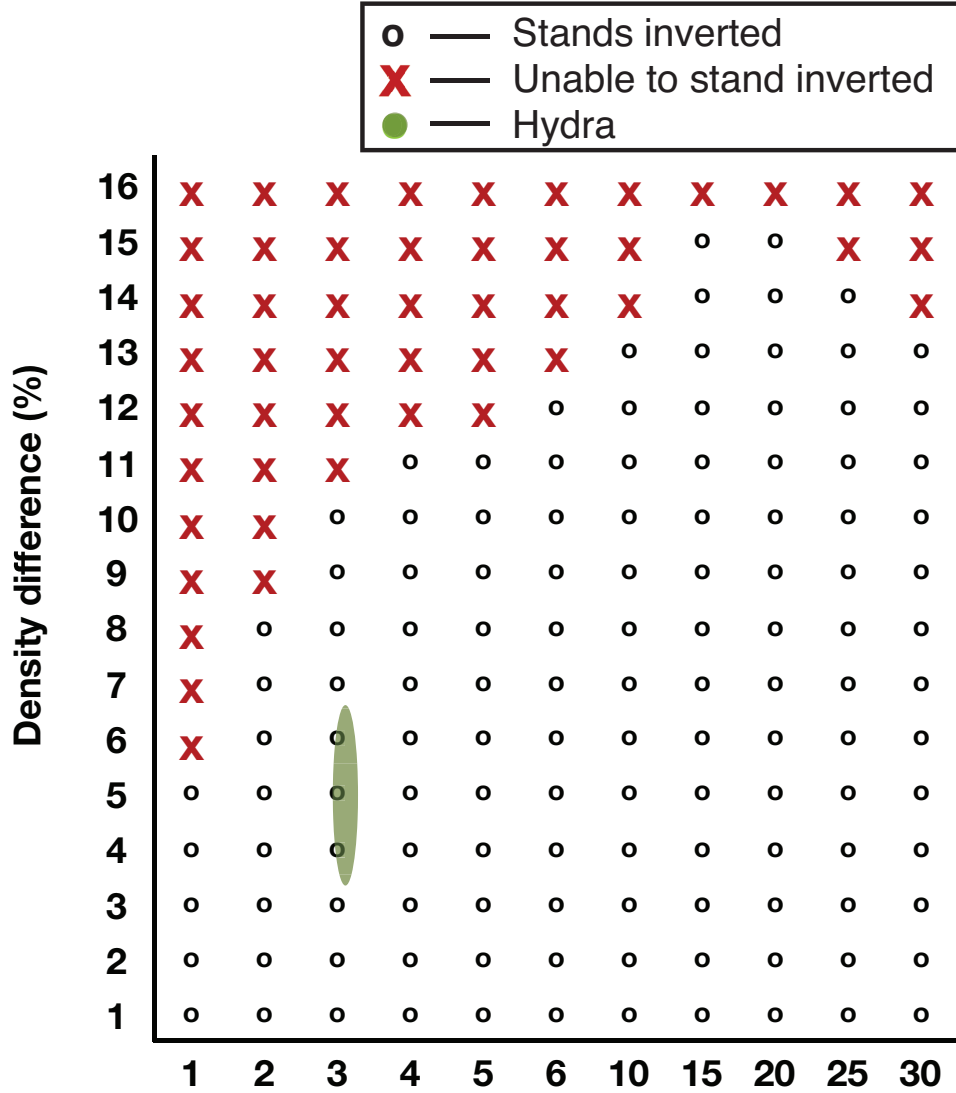


Figure 3.8: Phase diagram of model-Hydra's density difference (with respect to water) versus the Young's modulus ratio (α). The experimentally measured parameters of Hydra lie in the green oval in the phase space. The width and height of the oval represents errors involved in estimating α and Hydra density, respectively. The strain ϵ is 0.8.

fixed when the model Hydra is stretched, for $\alpha < 3$, Y for the body region is kept larger than 500 Pa. For $\alpha > 3$, the Y for the body region is kept smaller than 500 Pa. For $Y = 500$ Pa throughout the body column, it is not able to rise and stands inverted if the tissue is 2.5% denser than water. The parameters $\Delta\rho$ and α for real Hydra lie inside the green oval shape (fig 3.8).

The phase diagram is robust with respect to strain and different initial energies stored in the stretch. It indicates that a model Hydra with larger α , signifying a better energy transfer, can lift itself even if its heavy, which is described by a larger $\Delta\rho$. It is also interesting that the critical behaviour for lifting the body column is seen in the phase plot of $\Delta\rho$ and α only for the range of tissue stiffness seen in real Hydra.

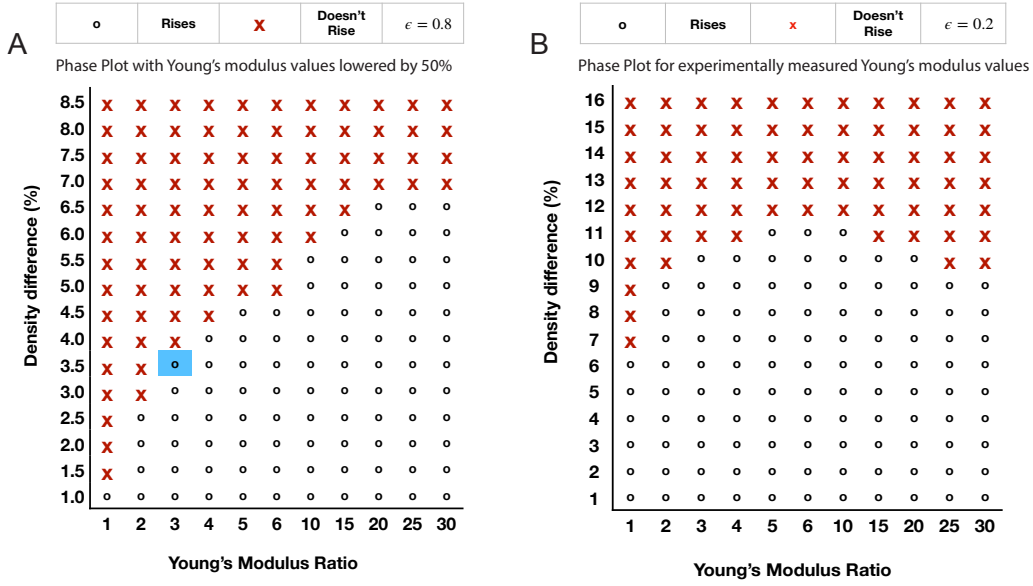


Figure 3.9: **A.** Phase diagram $\Delta\rho$ and α for $\epsilon = 0.8$ obtained with Young's modulus value half of experimentally observed values. The uniform stiffness ($\alpha = 1$) enables Hydra to lift the body column having density difference of only 1% compared to water. The blue square denotes the lower bound on density of real Hydra tissue and $\alpha = 3$. The plot underscores the importance of variation in stiffness even if it is overestimated in AFM measurements due to glutaraldehyde treatment. **B.** The phase diagram for strain $\epsilon = 0.2$. Note that the overall energy in the stretch is reduced due to smaller strains. The dissipated energy while the body column is contracting is much less too. Hence, the tissue stiffness variation is not very critical for the density difference of 6% and below. Albeit the Hydra with larger variation in tissue stiffness characterized by larger α is able to lift body columns with density difference of up to 9 – 10%.

The experimentally measured stiffness of Hydra tissue is likely to be an overestimate due to treatment of Glutaraldehyde. It has also been reported that such treatment does not largely affect tissue stiffness. It is difficult to quantify such effect in case of Hydra, but the observed increase in Young's

modulus due to such treatment on rat-tail tendons quantified using AFM is nearly 50% [27].

We have performed simulation runs to monitor the effect of such overestimations on the critical nature of standing upside down. fig 3.9-A shows a phase diagram in which, Y for both shoulder and body column is halved compared to the experimentally observed values in our AFM experiments. The variation characterized by α is seen to be more critical than that depicted in fig 3.8. Hydra with uniform stiffness is unable to lift its body column, even if it is 1% above the density of water.

The phase plot in fig 3.8 was for larger strain of $\epsilon = 0.8$. In fig 3.9-B, we have plotted the same for the lower value of strain, $\epsilon = 0.2$. We observed a small difference between these plots, as the density difference for the $\alpha = 3$ case shifts up by 1%.

Chapter 4

Conclusion and Remarks

Nature has a fascinating way of optimizing the efficiency of energy utilization in multiple cycles of evolution. We made an honest attempt to capture a small glimpse of such an optimization, by investigating a peculiar behaviour of stiffness along Hydra's body column.

We began by measuring Young's modulus along Hydra's body column. Hydra's body is small, about 5 mm in length. To resolve the Young's modulus along its surface, we used an AFM, together with the theory of contact mechanics by Hertz.

We observed a sharp gradient of Young's modulus values along the Hydra's body column. This was unexpected as Hydra's body seemed to be composed of the same cells from head to basal tip. We hypothesized a higher value of Young's modulus could possibly be responsible for a part of Hydra's somersault motion.

While having a stiffer base to pivot Hydra's body against viscous drag made some intuitive sense, it was unclear to us if such a gradient was necessary. In other words, if Hydras could complete their motion without such a gradient, why would they evolve one?

Furthermore, what was the significance of the stiffness gradient ratio of 3 : 1? If the hypothesis was correct, why would the Hydra not evolve a stiffer shoulder with the gradient ratio of say 10 : 1 or 20 : 1? Does 3 : 1 provide some special advantage that disappears for lower or higher values?

It is known that Hydra's elasticity is mostly governed by the ECM, or the Extra Cellular matrix. The ECM (also known as Mesoglea) is sandwiched between Hydra's Epithelial cells. To see if our hypothesis had any validity, we modulated this ECM using chemical and physical perturbations. Using these techniques, and the fact that Hydra has regenerative properties, we were able to create Hydra polyps with a uniform, constant stiffness from shoulder to basal tip.

We discovered that the Hydra with a uniform stiffness were unable to complete the somersault motion, thus giving a possible reason for the validity of the hypothesis.

To understand the underlying mechanics of the motion, we developed a physics-based computer simulation model of Hydra, with a minimal set of input parameters. After simulating several hydras with different stiffness ratios (α) between the shoulder and the basal region, we were able to note a clear advantage for a gradient in terms of energy utilization. We not only noted a 50% higher increase in power, we also saw an improvement in energy storage and transfer mechanisms.

Although our simulations indicated a clear advantage to be had for a stiffness gradient, all our models were able to complete their motion, unlike the experiments. At this point, we factored in the Hydra density, which we had so far assumed to be equal to the water in which it lived. Upon factoring the density, which was measured experimentally, our simulations showed that a uniform stiffness Hydra was unable to complete its motion while the one with a gradient was able to.

To understand why we did not observe a higher stiffness ratio (say $\alpha > 10$), we studied models with multiple values of α , ranging from $\alpha = 1$ (uniform) up to $\alpha = 30$. All our models showed that whatever advantage was gained for smaller ratios (between $\alpha > 2$ and $\alpha < 10$) started to either plateau (diminishing gains with increasing α), or started to decrease monotonically. The reason behind it was related to the fact that we compared all Hydras to be at the same initial energy. This meant that as we made the stiffer end more stiff, we had to keep reducing the stiffness of the longer basal end, resulting in the longer end having no stiffness to hold itself together.

4.1 Future perspective, drawbacks of the model and experiments

By performing experiments and simulations, we were able to measure the elasticity of Hydra to have a peculiar ratio of 3 : 1. We could also conclude that this number provides a significant advantage to Hydra than having no stiffness gradient at all.

Using our model, we were also able to put bounds on the ratio of 3 : 1, by looking at higher and lower ratios. From our simulations, we were able to establish that $\alpha \in [2, 5]$ was the most optimal case in terms of energy utilization. However, we were unable to pinpoint α to the experimentally observed value of $\alpha = 3$.

Following is a list of reasons we think may have led to this, including things which we can improve in the future, and reasons which we do not have control over.

1. **Hydra is a living organism:** Hydra’s motion involves both active and passive parts. At present, while there is positive evidence towards the fact that the contractile motion is mostly passive, we have not found a way to say it definitively.
2. **Fluid dynamics was not explicitly solved:** We did not use explicit Navier-Stokes equations for the moving boundary of Hydra. Instead, we assumed a constant drag which was an average of long thin cylinder moving along its transverse and longitudinal axis.
3. **Finite element method:** We used a mass-spring method instead of FEM, which may have more accurately replicated the experimentally observed motion. Our model, however, is much faster.
4. **Accuracy of experiments/Biological variations:** Not all Hydros have the exact same shape, size or mass. There is an inherent variation in dimensions and measurements due to Hydra being a living organism. For our models, we could only put an average value as an input, and this inherent variation may result in an inherent variation of the results, which could not be controlled.
5. **Composite function:** We were able to find several functions and plotted them against either time (t) or stiffness ratio α . Each of these functions put some bounds to what are viable stiffness ratios. The Power, $P(\alpha)$ versus α curve showed a peak and a plateau for $\alpha \in [2, 6]$, whereas the average force $F(\alpha)$ curve bounded $\alpha \in [2, 10]$. It may be possible that we find a function with multiple input parameters (including current functions themselves as input) ,which narrows this range even further.

In conclusion, we would like to say that while we were successful in highlighting the importance of the stiffness gradient, understand some of the mechanics involved and clarify how a much higher stiffness ratio is sub-optimal, we could still improve the simulations by using more complex techniques like FEM coupled with explicit fluid equations, and using multi-parameter functions which peak at or near the experimentally observed value of α .

Chapter 5

Additional work: Molecular Dynamics simulation scheme to study shear banding in worm-like micelles

5.1 Introduction

Shear is defined as the component of stress tensor, which is co-planar to the cross-section of a given material. Materials, depending on their internal molecular composition, respond very differently when such stress is applied to them.

Such a response to shear stress is captured by a modulus, which relates the components of applied shear, usually represented with σ , with the components of strain or strain rate ($\gamma/\dot{\gamma}$).

The response of a given material to shear stress is broadly categorized as either completely viscous, completely elastic, or a combination of the two, termed as viscoelastic response. A viscous response is seen in Newtonian fluid like water, where upon the application of shear, the stress is instantaneously dissipated in the fluid. In a broader context, an instantaneous dissipative response means that an applied shear stress relaxation time is zero. Similarly, the application of shear stress on elastic solids leads to a storage of energy instead of dissipation. Such a response to shear is termed an elastic response.

There are many ways to characterize shear response of a given material. Quantities like storage and loss modulus (G' , G''), viscosity (η), dynamic viscosity (η') etc are some of the different types of moduli used, depending upon the rheological conditions.

In general, it is known that for a completely viscous response, the applied shear stress is proportional to strain rate, while the elastic response has stress being proportional to strain. The stress versus strain rate equation for viscous liquid has fluid viscosity (η) as the proportionality constant, while the elastic response has Young's modulus (Y).

Viscoelastic response requires a more complex relation between applied shear stress and strain. Such response is commonly observed in Macromolecular systems like Polymer melts [28], Micelles ([29], [30], [31]), Gels [32] etc. In Rheology, such systems are usually characterized by probing the materials with an oscillatory strain and measuring the response. The oscillation frequency is varied to probe different relaxation modes of the given material. Phenomenological models, like Maxwell's model, are used to compute the storage and the loss modulus in such experiments. The details of Maxwell's model are provided in appendix D.

A viscoelastic system also shows other diverse set of phenomenon depending on its internal molecular structure and the amount of shear strain rate applied [33], [34], [35], [36]. When sheared at a certain rate, a viscoelastic material may show a reduction or increment in its measured viscosity. Such occurrences are termed as shear thinning and shear thickening, respectively [37], [38]. In some cases, a material could also divide itself into slow-moving and fast-moving layers or bands or different stresses and velocity profiles. This is known as the phenomenon of shear banding. In the present work, we focus on the shear banding, seen in worm-like micellar solutions.

A Micelle (fig 5.1-A) is an self-assembled aggregate of surfactant molecules in an aqueous solution [39]. Depending upon the concentration, micelles prefer to self-assemble into different shapes. Our work focuses on the micelles which assemble in long tubular shapes (fig 5.1-B), with a hydrophobic tail towards the inside and hydrophilic head at their surface. These are known as worm-like micelles [40], [41].

When a worm-like micellar solution is sheared beyond a critical stress, the fluid breaks up into two flow regions with two different strain-rates [41], [42], [43]. On gradually increasing externally applied strain rate ($\dot{\gamma}_1$) in the micellar solution in a rheometer, the measured stress keeps on increasing linearly initially with strain. However, beyond a critical value of strain rate (stress) e.g. $\dot{\gamma}_1(\sigma_c) = 14s^{-1}$ for CPCl-Hex micellar solution [42], one also observes that a part of the fluid flows with a shear rate $\dot{\gamma}_2(\sigma_c)$, which higher than $\dot{\gamma}_1(\sigma_c)$ and the values of measured shear-stress plateaus off.

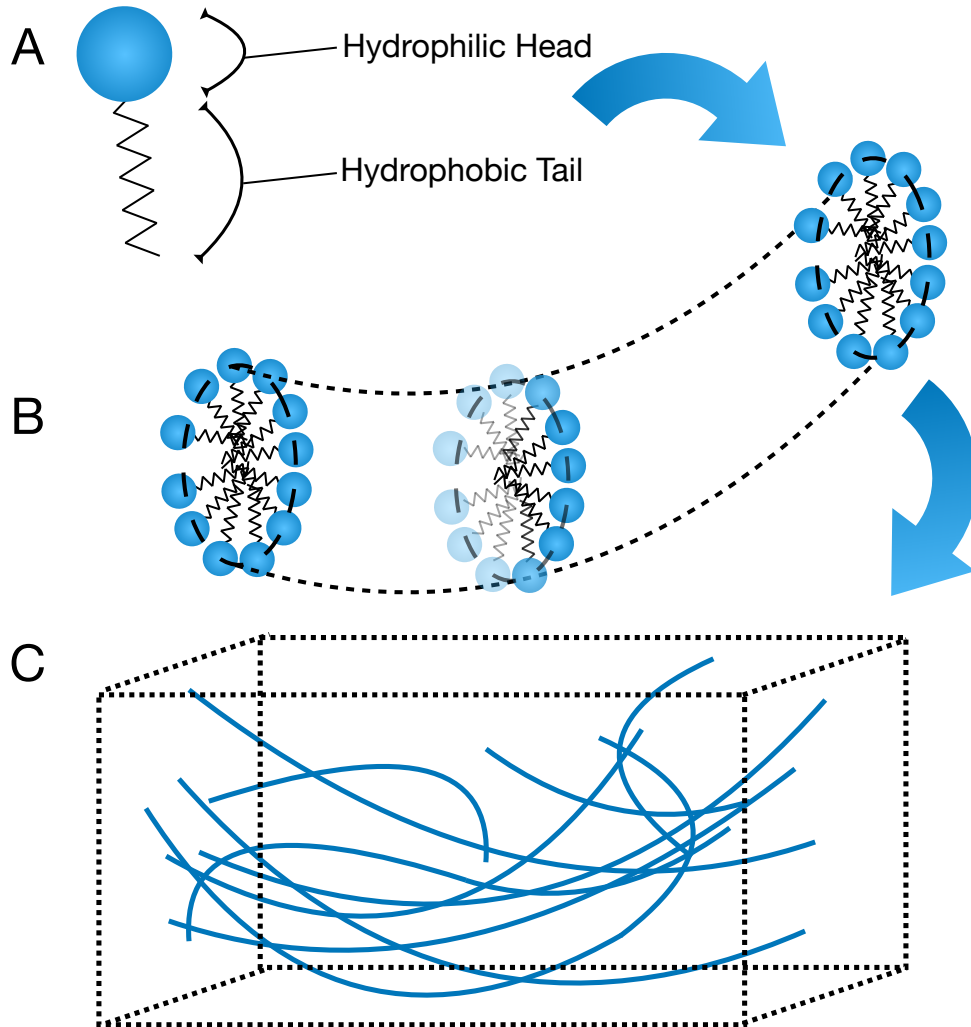


Figure 5.1: **A.** Micelle is an aggregate of surfactant molecule which consists of a hydrophilic head and a hydrophobic tail. **B.** At a certain concentration in an aqueous solution, micelles tend to self-assemble into long semi-flexible cylindrical aggregates, which is known as worm-like Micellar configuration. **C.** Many such worm-like micelles interact with each other in an aqueous medium. Such a configuration is known to exhibit characteristics of shear banding.

5.2 Chapter outline

We begin by describing the model used for performing the shear simulations in section [5.3](#). We discuss the types of particles in the model and the interaction potentials used. We then proceed to describe the simulations performed

in detail in section 5.4. We divide this section into two parts, the first being the initialization of the system while the other deals with the application of a constant strain rate. We end this chapter by briefly describing the preliminary results obtained by analysing the steady-state conditions of the shear flow. We report the first time observation of shear bands in a molecular dynamics simulations of worm-like micelles in this section.

5.3 Details of the Simulation Model

Our model, which was proposed by Dr. Apratim Chatterji and Alex Abraham, has been published in a previous work [44]. The previous work dealt with the equilibrium properties of self-assembling polymeric system. In particular, it was established that linear polymeric chains could be obtained using spherically symmetric potentials. In the present work, we use this model and analyse its steady-state properties under shear.

The model consists of two types of monomers, labelled as type-A and type-B. The interaction potential between A-A, and B-B is purely repulsive and is of the form

$$V_{AA}(r) = V_{BB}(r) = \epsilon_{\alpha\alpha} \frac{e^{-r/R_{\alpha\alpha}}}{r}, \forall r < r_c \quad (5.1)$$

This potential is also known as a screened Coulomb or a Yukawa potential. Here, the range of interaction is controlled by the parameter R , while the relative strength is controlled by the value of $\epsilon_{\alpha\alpha}$.

The interaction between A-B can be divided into three parts based on the distance between the particles. At very short distances, we expect the particles to repel each other similar to a hard-sphere. This is modelled by an excluded volume term $\sim (\sigma/r)^{24}$. Here, r is the distance between the two particles, and σ is the diameter of the particle. The second part takes care of short-range attraction. These include distances just slightly more than the particle diameter (σ , fig 5.2). We use the term $\sim -(\sigma/r)^{12}$ to model this attractive part. The third part of the interaction is the screened Coulomb interaction term, $\sim e^{-r/R}/r$. The interaction range for the screened Coulomb potential is decided by the value of R . The relative strength of the screened Coulomb potential is controlled by the constant ϵ_{AB}^* , while the relative combined strength of the excluded volume and short-range attractive term is controlled by a single constant ϵ_{AB}

$$V_{AB}(r) = \epsilon_{AB} \left[\left(\frac{\sigma}{r} \right)^{24} - \left(\frac{\sigma}{r} \right)^{12} \right] + \epsilon_{AB}^* \frac{e^{-r/R_{AB}}}{r} \quad (5.2)$$

We again note that all the terms in both V_{AB} and V_{AA}, V_{BB} only depend on the radial distance between monomers, and are thus spherically symmetric. As discussed above, linear polymeric chains were obtained using these potentials. This eliminated the need of calculating more computationally expensive and time-consuming 3 or 4 body potentials to model semi-flexible polymer chains. Thus permitting the study of larger systems for longer periods. The parameter σ in the simulations is also known as the "excluded volume distance". It is the unit of length in the simulations and is set to $\sigma = 1$. All the energies in the simulations henceforth are measured in terms of unit thermal energy $k_B T$. The $k_B T$ is also set to unity. The unit of mass (m) is also set to unity, with monomers of both types having a mass of $m = 1$. We can construct the simulation time τ by combining $k_B T, \sigma$ and m , as $\tau = \frac{1}{\sigma} \sqrt{\frac{m}{k_B T}} = 1$.

The range of the potential $V_{AA}(r)$, which is controlled by the parameter $R_{\alpha\alpha}$ is set to $R_{\alpha\alpha} = 2.30\sigma$, while the range of $V_{AB}(r)$ is set to $R_{AB} = 1.9\sigma$. The combined strength of the excluded volume and short-range attraction, is also set to a constant value throughout the simulations as $\epsilon_{AB} = 113.4k_B T$. The constant associated strength of the screened Coulomb potential for V_{AB} potential is defined as ϵ_{AB}^* in eq 5.2. However, it needs to be noted that for V_{AB} , the screened Coulomb is shifted horizontally by r_0 , to accommodate for the excluded volume and the short-range attraction terms. ϵ_{AB}^* is obtained by multiplying the Coulomb strength ϵ_{AB}^c by an exponential constant term $e^{r_0/R_{AB}}$. Thus we have $\epsilon_{AB}^* = \epsilon_{AB}^c e^{r_0/R_{AB}}$. More explicitly, the Coulomb term in eq 5.2 can be written as $\epsilon_{AB}^* \frac{e^{-r/R_{AB}}}{r} = \epsilon_{AB}^c e^{r_0/R_{AB}} \frac{e^{-r/R_{AB}}}{r} = \epsilon_{AB}^c \frac{e^{-(r-r_0)/R_{AB}}}{r}$. In the simulations, $r_0 = 1.12\sigma$ and $\epsilon_{AB}^c = 23.10k_B T$.

The parameter $\epsilon_{\alpha\alpha}$ controls the strength of screened Coulomb repulsion of particles of same type ($V_{AA} = V_{BB}$). This parameter is also responsible for branching. The simulations have been conducted for several different values of $\epsilon_{\alpha\alpha}$, ranging from $\epsilon_{\alpha\alpha} = 1.25 \times 10^5 k_B T$ to $\epsilon_{\alpha\alpha} = 5.00 \times 10^5 k_B T$, to check for shear banding. For each value of $\epsilon_{\alpha\alpha}$, we also analysed the steady-state properties at different shear rates, ranging from $\dot{\gamma} = 0.005$ to $\dot{\gamma} = 0.02$, and we also varied the monomer densities from $\rho = 0.150$ to $\rho = 0.165$. We used a box size of $90 \times 30 \times 30\sigma^3$, with x -axis to be the longer, shear direction. Periodic boundary conditions were incorporated in the x and y directions, while solid walls are present along the z -axis.

The time evolution of the simulation is carried out using the velocity verlet integration method in molecular dynamics. Additionally, we have included an implicit fluid by combining the velocity verlet with a langevin dynamics. The langevin noise, which is given by the fluctuation-dissipation theorem as, $\langle \eta(t)\eta(t') \rangle = 2\Gamma k_B T \delta(t - t')$, is taken to be $\Gamma = 0.1$.

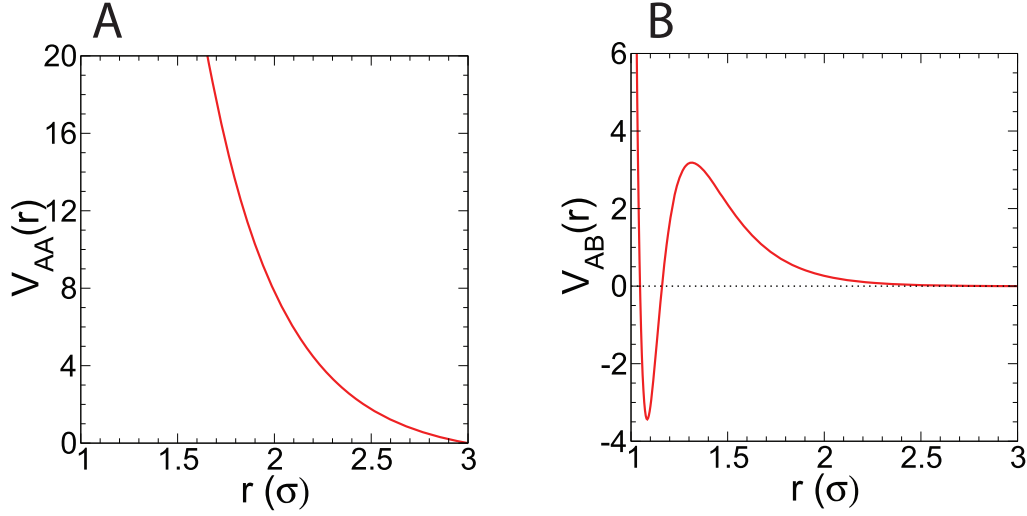


Figure 5.2: **A.** Potential between similar monomers, A-A or B-B (denoted by $V_{AA}(r)$) is plotted versus the radial distance between them $r(\sigma)$. **B.** Potential $V_{AB}(r)$ is the potential between particles of type A and B, plotted as a function of radial distance ($r(\sigma)$) between them. Both $V_{AA}(r)$ and $V_{AB}(r)$ are spherically symmetric potentials.

5.4 Simulations

5.4.1 System initialization and equilibration

We begin the simulations with a box size of $90 \times 30 \times 30\sigma^3$, with $l_x = 90\sigma$ being the direction of shear. Initially, we do not apply any shear to the system and let it settle in an equilibrium configuration. The system is initialized for a given density such that the monomers of type-A and type-B are distributed homogeneously across the simulation box. The number of monomers of type-A is kept to be exactly the same as type-B. This is done to ensure that the inhomogeneities arising during the course of the simulations are only due to interaction potential and not due to unequal distribution of monomers of different types. During this initialization step, we apply periodic boundary conditions in all three directions.

5.4.2 Application of strain rate

Once equilibrium is reached, we re-initialize the system starting from the final equilibrium configuration achieved during the initialization steps. We define walls of equal thickness at both ends of the l_z direction. Any monomer

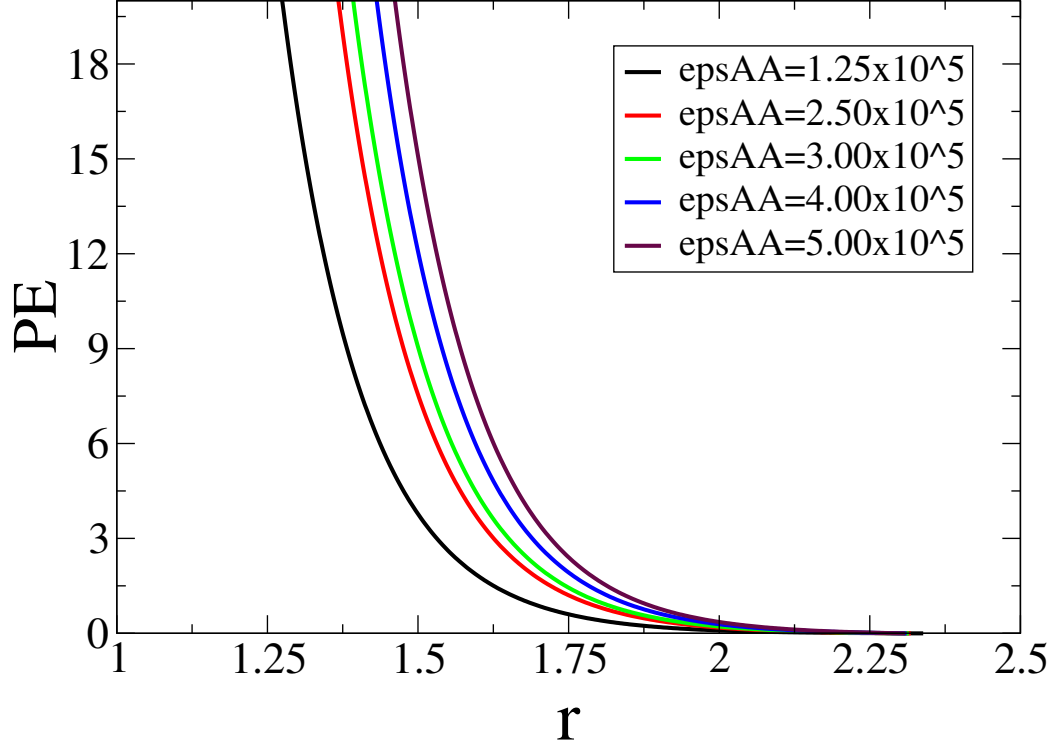


Figure 5.3: The simulations were performed for several values of $\epsilon_{\alpha\alpha}$, which controls the strength of the Coulomb repulsion of particles of the same type. $V_{AA}(r)$ is plotted as a function of radial separation between particles for different values of $\epsilon_{\alpha\alpha}$

of either type, which ends up within these walls, is frozen. Furthermore, if a monomer finds its way in either the top or the bottom section from the bulk during the simulations, it is also frozen in its place and begins to move with the velocity derived from the strain rate assigned to the top or the bottom section.

The positions and the velocities of monomers within the bulk are updated according to the velocity-verlet algorithm, which is typical in a molecular dynamics simulation. These equations are:

$$r_i^{n+1} = r_i^n + \Delta_t v_n + \frac{1}{2} \Delta_t^2 a_n \quad (5.3)$$

$$v_i^{n+1} = v_i^n + \frac{1}{2} \Delta_t (a_{n+1} + a_n) \quad (5.4)$$

Additionally, we include an implicit fluid, which the particles interact with. This is modelled by including a dissipation and a noise term, commonly known together as langevin dynamics. The dissipation term is Γ , and its

strength in our simulations is set to $\Gamma = 0.1$. Once the dissipation constant is fixed, the amplitude of the noise term $\eta(t)$, is also fixed using the fluctuation dissipation theorem,

$$\langle \eta(t)\eta(t') \rangle = 2\Gamma k_B T \delta(t - t') \quad (5.5)$$

These additional terms are included by modifying the velocity verlet algorithm (see appendix [B](#)).

We begin the simulations by assigning a constant strain rate ($\dot{\gamma}$) to the top section, while the bottom section is stationary (blue regions in [fig 5.4](#)). Unlike the initialization phase, however we apply periodic boundary conditions only along the x and the y -axis, while the z direction is bounded by the top and bottom walls.

When we apply an external force on the top layer for shear, we need to ensure that the temperature profile across the simulation remains constant (isothermal condition). For this, we use a layer-wise thermostat in our simulations. This is implemented in the following way: First, we divide the simulation into multiple layers of unit length each. Since the combined wall thickness in the simulations is 5σ , we are left with a bulk thickness of 25σ , which leaves us with 25 layers. For each layer, we calculate the total kinetic energy, from the set of velocities of the particles $\{v'_1, v'_2 \dots v'_{N_L}\}$, where N_L is the number of particles in a given layer L . According to the equipartition theorem, the total kinetic energy in a given layer must be equal to the total number of particles within that layer,

$$\frac{1}{2} \sum_{i=1}^{N_L} m_i v_i^2 = \frac{3}{2} k_B T N_L \quad (5.6)$$

Therefore, we must find a constant factor, with which we can scale the velocities of the particles with a given layer L , such that the total kinetic energy satisfies the equipartition theorem. In particular, we need to find a scale factor ξ_L , such that when $v_i = \xi_L \times v'_i$, we get

$$\frac{1}{2} \sum_{i=1}^{N_L} m_i \xi_L^2 v_i'^2 = \frac{3}{2} k_B T N_L \quad (5.7)$$

From here, we can find the value of ξ to be

$$\xi_L = \sqrt{\frac{3k_B T N_L}{\sum_{i=1}^{N_L} m_i v_i'^2}} \quad (5.8)$$

Therefore for every layer, we find the value of ξ_L , and scale the velocities. To verify the thermostat, we also measured the temperature profile versus the z-axis. We observed a constant average temperature across all layers during the steady-state.

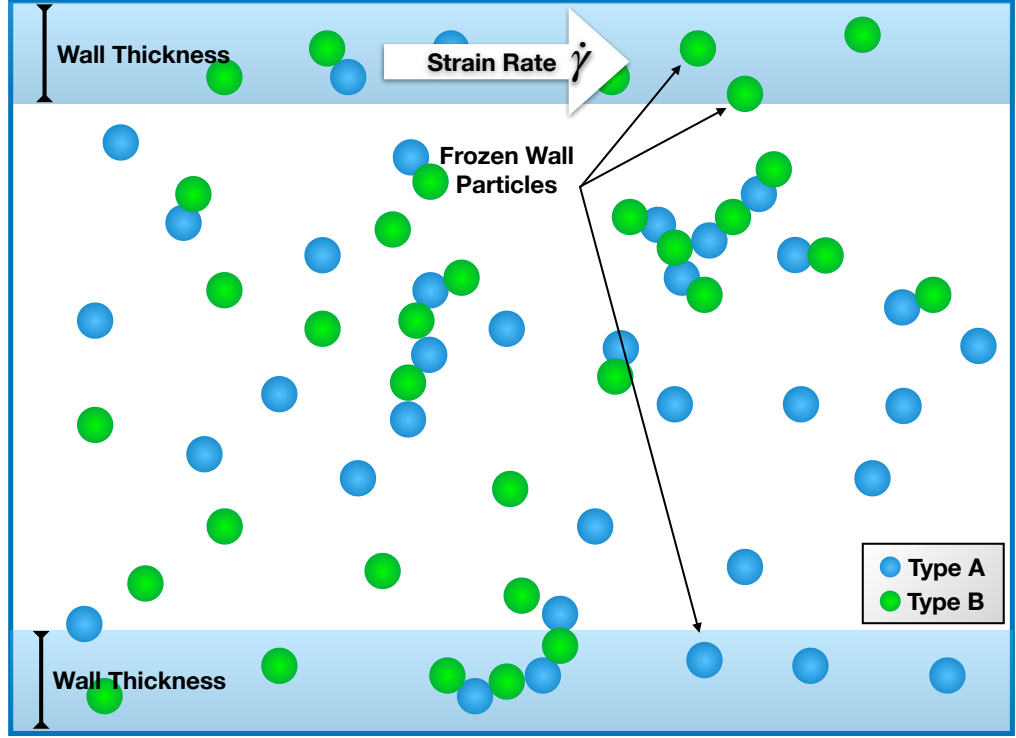


Figure 5.4: Representation of a cross-section of simulation box, along the vertical l_y and horizontal l_x axis. The simulation box is divided into three sections after equilibrium is reached. Monomers which end up in the top or the bottom section (in the blue region) after equilibrium are frozen in their place, while the middle section is called "bulk." Monomers in bulk region are propagated in time according the usual velocity verlet algorithm coupled with langevin noise. All the monomers in the top wall (section) are displaced with a constant strain rate. This effectively shears the system, and we extract the results once a steady state is reached.

5.5 Result and discussions

We calculated the velocity profile of the micellar system along the z axis. This was done in the following way:

We first divide the bulk into layers of unit length along the z axis. Since the cumulative wall thickness is 5σ , we are left with 25 layers in bulk. We calculate the centre of mass velocity of each layer after every 20 iterations and average it over every 10^5 iterations/time steps in the simulations. We start this averaging procedure after rejecting the first 20×10^5 iterations, to ensure that the steady-state is reached. We utilize a similar procedure to calculate other quantities like temperature and density profiles.

A linear velocity profile is expected when no shear bands are present in the simulations. However, in the presence of shear banding, we would expect the bulk monomers to split themselves into two or more bands moving with different velocities. This would be a deviation from the linear velocity profile.

In our simulations, we explored a combination of different shear rates, values of $\epsilon_{\alpha\alpha}$, and different densities. We report for the first time, the observation of shear bands in a molecular dynamics simulation, for specific values of $\epsilon_{\alpha\alpha} = 2.5 \times 10^5$, monomer density of 0.160 and the shear rate of 0.01. In fig [5.5-B](#), a clear deviation from the dashed linear velocity profile could be seen. Such a deviation is the first indication of the presence of shear banding present in the system.

We also note the upper part of the curve in [5.5-B](#), with $z < 5\sigma$, shows a velocity that is faster than the externally applied velocity of the top layer. This is also a sign of shear bands in micellar solutions, where the fast-moving phase is faster than the applied shear rate [41](#).

5.6 Conclusion and future perspective

In the present work, we have reported the first observation of shear banding in worm-like micelles using molecular dynamics simulations. For this, we used novel, two-body spherically-symmetric potentials, which helped reduce computationally expensive calculations.

In future, we would like to develop a more microscopic level understanding of our simulations. This could be done by calculating bond extension within different layers, bond alignments, branching etc. We would also like to calculate the full stress tensor in every layer.

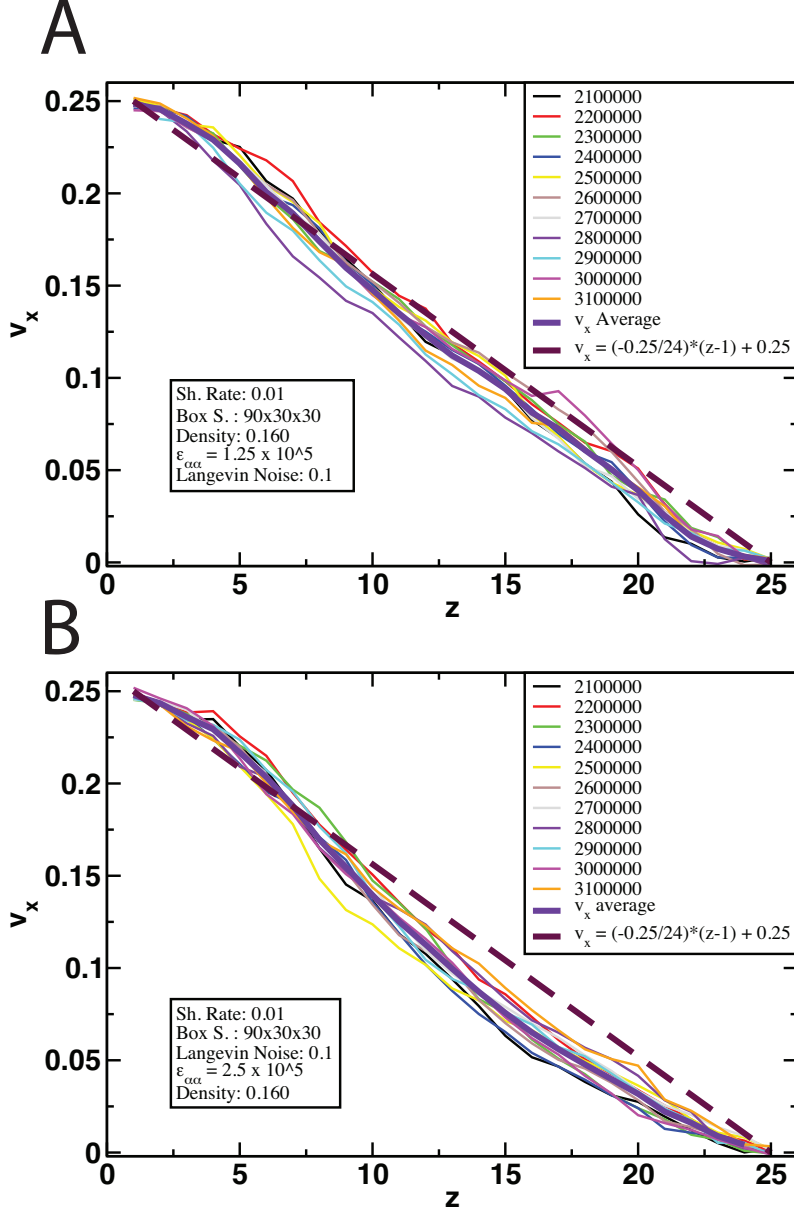


Figure 5.5: **A.** Velocity in the x direction v_x is plotted along the z -axis for $\epsilon_{\alpha\alpha} = 1.25 \times 10^5$. **B.** Velocity v_x is plotted along the z -axis for $\epsilon_{\alpha\alpha} = 2.5 \times 10^5$. In both cases, the langevin noise amplitude is set to 0.1, with the particle density of 0.160 and shear rate $\dot{\gamma} = 0.01$. The solid purple line represents the average of each of the velocity curves, while the dashed line is the expected linear velocity profile when no shear banding is present. In **B**, we can see a clear deviation from the dashed line, which is indicative of a shear banded flow.

References

- [1] G. H. Orians, Age and hunting success in the brown pelican (*pelecanus occidentalis*), *Animal Behaviour* 17 (1969) 316–319 (1969).
- [2] C. Von Beeren, A. K. Tishechkin, *Nymphister kronaueri* von beeren & tishechkin sp. nov., an army ant-associated beetle species (coleoptera: Histeridae: Haeteriinae) with an exceptional mechanism of phoresy, *BMC Zoology* 2 (1) (2017) 3 (2017).
- [3] F.-S. Chia, J. Buckland-Nicks, C. M. Young, Locomotion of marine invertebrate larvae: a review, *Canadian Journal of Zoology* 62 (7) (1984) 1205–1222 (1984).
- [4] A. Biewener, S. Patek, *Animal locomotion*, Oxford University Press, 2018 (2018).
- [5] M. C. Day, et al., *Spider wasps: Hymenoptera: Pompilidae.*, Vol. 6, Royal Entomological Society, 1988 (1988).
- [6] R. Aufschnaiter, R. Wedlich-Söldner, X. Zhang, B. Hobmayer, Apical and basal epitheliomuscular f-actin dynamics during hydra bud evagination, *Biology open* 6 (8) (2017) 1137–1148 (2017).
- [7] J. F. Haynes, A. L. Burnett, L. E. Davis, Histological and ultrastructural study of the muscular and nervous systems in hydra. i. the muscular system and the mesoglea, *Journal of Experimental Zoology* 167 (3) (1968) 283–293 (1968).
- [8] G. Mackie, Locomotion, flotation, and dispersal, in: *Coelenterate Biology: Reviews and New Perspectives*, Academic Press New York, 1974, pp. 313–357 (1974).
- [9] W. Hu, G. Z. Lum, M. Mastrangeli, M. Sitti, Small-scale soft-bodied robot with multimodal locomotion, *Nature* 554 (7690) (2018) 81–85 (2018).

- [10] G. A. Cavagna, N. C. Heglund, C. R. Taylor, Mechanical work in terrestrial locomotion: two basic mechanisms for minimizing energy expenditure, *American Journal of Physiology-Regulatory, Integrative and Comparative Physiology* 233 (5) (1977) R243–R261 (1977).
- [11] R. Akhtar, M. J. Sherratt, J. K. Cruickshank, B. Derby, Characterizing the elastic properties of tissues, *Materials Today* 14 (3) (2011) 96–105 (2011).
- [12] R. C. Siegel, S. R. Pinnell, G. R. Martin, Cross-linking of collagen and elastin. properties of lysyl oxidase, *Biochemistry* 9 (23) (1970) 4486–4492 (1970).
- [13] H. Shimizu, R. Aufschnaiter, L. Li, M. P. Sarras Jr, D.-B. Borza, D. R. Abrahamson, Y. Sado, X. Zhang, The extracellular matrix of hydra is a porous sheet and contains type iv collagen, *Zoology* 111 (5) (2008) 410–418 (2008).
- [14] H. Shimizu, X. Zhang, J. Zhang, A. Leontovich, K. Fei, L. Yan, M. P. Sarras, Epithelial morphogenesis in hydra requires de novo expression of extracellular matrix components and matrix metalloproteinases, *Development* 129 (6) (2002) 1521–1532 (2002).
- [15] M. P. Sarras Jr, D. Meador, X. Zhang, Extracellular matrix (mesoglea) of hydra vulgaris: Ii. influence of collagen and proteoglycan components on head regeneration, *Developmental biology* 148 (2) (1991) 495–500 (1991).
- [16] L. Landau, E. Lifshitz, *Elasticity theory* (1987).
- [17] M. Kellomäki, J. Åström, J. Timonen, Rigidity and dynamics of random spring networks, *Physical review letters* 77 (13) (1996) 2730 (1996).
- [18] J. A. Åström, J. Mäkinen, M. J. Alava, J. Timonen, Elasticity of poissonian fiber networks, *Physical Review E* 61 (5) (2000) 5550 (2000).
- [19] L. Berlyand, A. G. Kolpakov, A. Novikov, *Introduction to the network approximation method for materials modeling*, Vol. 148, Cambridge University Press, 2013 (2013).
- [20] J. K. Dhont, *An introduction to dynamics of colloids*, Elsevier, 1996 (1996).

- [21] J. E. Jones, On the determination of molecular fields.—ii. from the equation of state of a gas, *Proceedings of the Royal Society of London. Series A, Containing Papers of a Mathematical and Physical Character* 106 (738) (1924) 463–477 (1924).
- [22] J. D. Weeks, D. Chandler, H. C. Andersen, Role of repulsive forces in determining the equilibrium structure of simple liquids, *The Journal of chemical physics* 54 (12) (1971) 5237–5247 (1971).
- [23] D. Frenkel, B. Smit, *Understanding molecular simulation: from algorithms to applications*, Vol. 1, Elsevier, 2001 (2001).
- [24] A. Gooneie, S. Schuschnigg, C. Holzer, A review of multiscale computational methods in polymeric materials, *Polymers* 9 (1) (2017) 16 (2017).
- [25] F. Jabbari, A. Rajabpour, S. Saedodin, Thermal conductivity and viscosity of nanofluids: a review of recent molecular dynamics studies, *Chemical Engineering Science* 174 (2017) 67–81 (2017).
- [26] N. Grønbech-Jensen, O. Farago, A simple and effective verlet-type algorithm for simulating langevin dynamics, *Molecular Physics* 111 (8) (2013) 983–991 (2013).
- [27] P. Hansen, T. Hassenkam, R. B. Svensson, P. Aagaard, T. Trappe, B. T. Haraldsson, M. Kjaer, P. Magnusson, Glutaraldehyde cross-linking of tendon—mechanical effects at the level of the tendon fascicle and fibril, *Connective tissue research* 50 (4) (2009) 211–222 (2009).
- [28] J. Cao, A. E. Likhtman, Shear banding in molecular dynamics of polymer melts, *Physical review letters* 108 (2) (2012) 028302 (2012).
- [29] C. R. López-Barrón, A. K. Gurnon, A. P. Eberle, L. Porcar, N. J. Wagner, Microstructural evolution of a model, shear-banding micellar solution during shear startup and cessation, *Physical Review E* 89 (4) (2014) 042301 (2014).
- [30] M. E. Cates, S. M. Fielding, Rheology of giant micelles, *Advances in Physics* 55 (7-8) (2006) 799–879 (2006).
- [31] A. K. Gurnon, C. R. Lopez-Barron, A. P. Eberle, L. Porcar, N. J. Wagner, Spatiotemporal stress and structure evolution in dynamically sheared polymer-like micellar solutions, *Soft matter* 10 (16) (2014) 2889–2898 (2014).

- [32] Z. Chu, Y. Feng, Amidosulfobetaine surfactant gels with shear banding transitions, *Soft Matter* 6 (24) (2010) 6065–6067 (2010).
- [33] H. Rehage, H. Hoffmann, Rheological properties of viscoelastic surfactant systems, *The Journal of Physical Chemistry* 92 (16) (1988) 4712–4719 (1988).
- [34] H. Rehage, H. Hoffmann, Viscoelastic surfactant solutions: model systems for rheological research, *Molecular Physics* 74 (5) (1991) 933–973 (1991).
- [35] S. M. Fielding, Complex dynamics of shear banded flows, *Soft Matter* 3 (10) (2007) 1262–1279 (2007).
- [36] B. Chakrabarti, M. Das, C. Dasgupta, S. Ramaswamy, A. Sood, Spatiotemporal rheochaos in nematic hydrodynamics, *Physical review letters* 92 (5) (2004) 055501 (2004).
- [37] T. Divoux, M. A. Fardin, S. Manneville, S. Lerouge, Shear banding of complex fluids, *Annual Review of Fluid Mechanics* 48 (2016) 81–103 (2016).
- [38] P. D. Olmsted, Perspectives on shear banding in complex fluids, *Rheologica Acta* 47 (3) (2008) 283–300 (2008).
- [39] C. Tanford, Micelle shape and size, *The Journal of Physical Chemistry* 76 (21) (1972) 3020–3024 (1972).
- [40] J. Yang, Viscoelastic wormlike micelles and their applications, *Current opinion in colloid & interface science* 7 (5-6) (2002) 276–281 (2002).
- [41] R. Mair, P. Callaghan, Observation of shear banding in worm-like micelles by nmr velocity imaging, *EPL (Europhysics Letters)* 36 (9) (1996) 719 (1996).
- [42] J.-F. Berret, Rheology of wormlike micelles: Equilibrium properties and shear banding transitions, in: *Molecular gels*, Springer, 2006, pp. 667–720 (2006).
- [43] S. Lerouge, J.-F. Berret, Shear-induced transitions and instabilities in surfactant wormlike micelles, in: *Polymer Characterization*, Springer, 2009, pp. 1–71 (2009).
- [44] A. Abraham, A. Chatterji, Self assembled linear polymeric chains with tuneable semiflexibility using isotropic interactions, *The Journal of chemical physics* 148 (15) (2018) 154901 (2018).

Appendix A

Exponential nature of bending energy E_{bend} with Time (t)

It is slightly tricky to separate two different forms of energy stored in our simulations. One is the energy during the contractile motion, while the other is the "bending" energy stored in the shoulder region after the contraction ends.

Since our simulations involve beads and springs, and we only have access to the potential energies stored in such springs, we can not tell the difference between the "bending" and the "stretching" energy.

However, as discussed in chapter 1, to show that the contraction and upward motion of hydra is mostly passive, involves establishing the exponential nature of the the dissipation of bending energy. In this appendix, we show this trend both in the experiments, and try to replicate it in the simulations.

For a bent cylinder/rod, the energy stored in the "bend" is proportional to the cylinder's Young's modulus and it's curvature.

$$U \propto \frac{YIL}{2R^2} \quad (\text{A.1})$$

Where, I is the second moment of area and R is the curvature

$$I = \int y^2 dA \quad (\text{A.2})$$

To show that this energy has an exponential trend, it is enough to calculate the curvature of the bent shoulder region of Hydra and plotting its inverse squared with time. This is plotted in the fig [A.1](#)

In [A.1](#) it can be seen that during the initial contraction, the shoulder region is flat, thus its curvature is zero, thus the bending energy is also zero. As the contraction occurs, the shoulder becomes more and more curved, thus

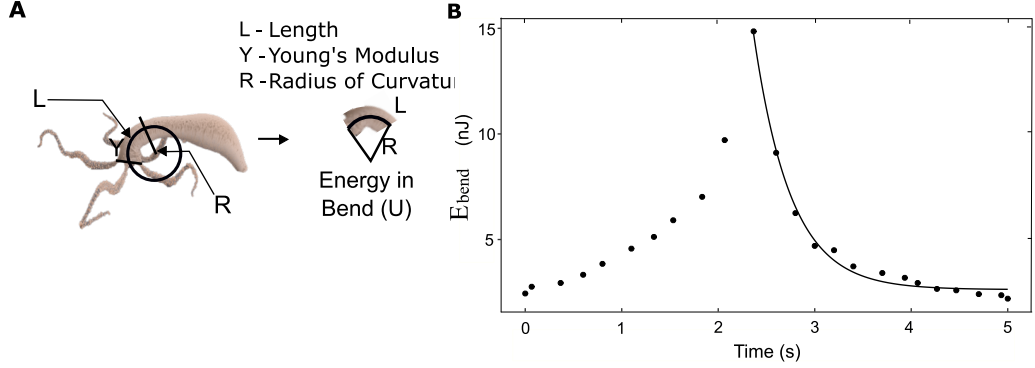


Figure A.1: Experimentally measured bending energy curve shows an exponential trend with time. Exact value of the constant of proportionality could not be established thus there is a slight discrepancy between the absolute values from the experiments and simulations.

storing larger bending energy. There is a clear peak of E_{bend} , which marks the maximum possible curvature of the shoulder region, and the start of the upward motion. The points from max E_{bend} till the end of the motion show a definite exponential decay trend, and fit well with the exponential curve (solid line)

Similar curve can also be replicated in our simulations by the following procedure. In our simulations, the first 14 circles (rings) out of the total 50, constitute of the stiffer shoulder region. We calculate the centre of mass of each of these rings to get 14 points, to get a set of (x, y) coordinates at a given time t_i , $\{[x_1(t_i), y_1(t_i)], [x_2(t_i), y_2(t_i)], \dots, [x_N(t_i), y_N(t_i)]\}$. We can estimate the radius of curvature by using the method of least square fit for a circle, defined by

$$\beta(t_i) = u_c^2(t_i) + v_c^2(t_i) + \frac{S_{uu} + S_{vv}}{N} \quad (A.3)$$

Where N is the total set of coordinates for a given time (14 in our case), u_c and v_c are the centre of curvature of the fit circle. u_c and v_c are found from by solving the matrix equation

$$\begin{bmatrix} S_{uu} & S_{uv} \\ S_{uv} & S_{vv} \end{bmatrix} \begin{bmatrix} u_c \\ v_c \end{bmatrix} = \frac{1}{2} \begin{bmatrix} S_{uuu} + S_{uvv} \\ S_{vvv} + S_{vu u} \end{bmatrix} \quad (A.4)$$

Where $S_u = \sum_i u_i$, $S_{uuu} = \sum_i u_i^3$, $S_{uuv} = \sum_i u_i^2 v_i$ etc.

The radius of curvature of the fit circle at a given time is then given by

$$R(t) = \sqrt{\beta(t)} \quad (A.5)$$

We repeated this analysis for different model-Hydra cases which have been plotted in fig A.2. The exponential decay trend can be clearly seen in all three plots. Just like the experiments, it can be seen that the initial bending energy is zero, since the entire body column of hydra is stretched. It increases rapidly as more and more energy from the stretched region is transferred to the shoulder. The figure also shows that the energy transfer and storage is better in the $\alpha = 3$ case, despite same initial energy.

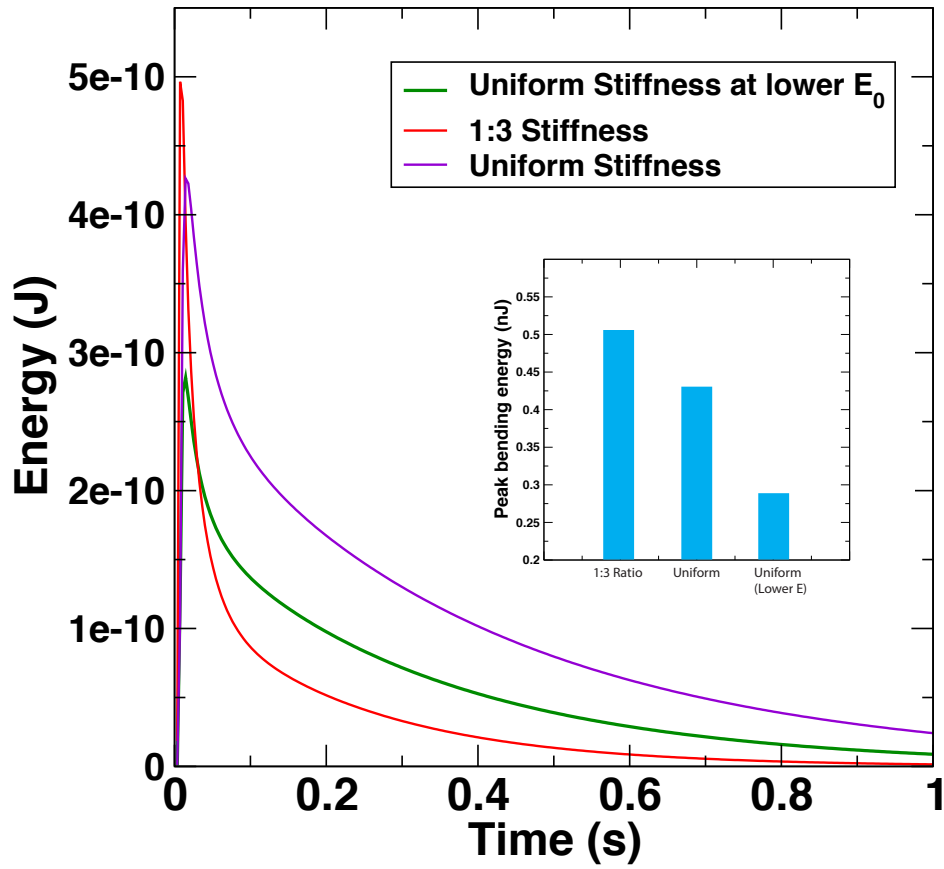


Figure A.2: Figure shows three different model-Hydra plots. The gradient ($\alpha = 3$) clearly shows a larger peak bending energy than the and the uniform ($\alpha = 1$). We also simulated a uniform $\alpha = 1$ model at a lower energy, to match the experiments

Appendix B

Velocity Verlet algorithm in Damped condition

The velocity verlet method of integration, is given by the following set of equations

$$x_{n+1} = x_n + \Delta_t v_n + \frac{1}{2} \Delta_t^2 a_n, \quad (\text{B.1})$$

$$v_{n+1} = v_n + \frac{1}{2} \Delta_t (a_{n+1} + a_n) \quad (\text{B.2})$$

The formulation is made under the assumption that the acceleration/force is strictly dependent only on the position, i.e. $f = f(x_n, t_n)$.

In case of damping, the force and the acceleration take the form

$$f \rightarrow f(x_n, v_n, t_n) \quad (\text{B.3})$$

$$a \rightarrow a(x_n, v_n, t_n) \quad (\text{B.4})$$

Due to the v_n dependency of the acceleration, it becomes difficult to evaluate v_{n+1} as equation [B.2](#) itself depends on v_{n+1}

$$v_{n+1} = v_n + \frac{1}{2} \Delta_t [a_{n+1}(x_{n+1}, v_{n+1}, t_{n+1}) + a_n(x_n, v_n, t_n)] \quad (\text{B.5})$$

To resolve this problem, we begin by approximating $a_{n+1} = a(x_{n+1}, v_{n+1}, t_{n+1})$ by $a_{n+1} = a(x_{n+1}, v_n + a_n \Delta_t, t_{n+1})$ and then refining. Using this in the velocity verlet equations [B.1](#) [B.2](#), we get following set of equations:

$$x_{n+1} = x_n + \Delta_t v_n + \frac{1}{2} \Delta_t^2 a_n, \quad (\text{B.6})$$

$$\hat{v}_{n+1} = v_n + \frac{1}{2} \Delta_t [a_n + a(x_{n+1}, v_n + \Delta_t a_n, t_{n+1})], \quad (\text{B.7})$$

$$v_{n+1} = v_n + \frac{1}{2} \Delta_t [a_n + a(x_{n+1}, \hat{v}_{n+1}, t_{n+1})] \quad (\text{B.8})$$

This expression can be simplified by including the explicitly expression for the acceleration in case of linear damping. The linear damping formula can be written both in forward and backward difference method as:

$$G^F(v) = \gamma v = \frac{x_{n+1} - x_n}{\Delta_t} \quad (\text{B.9})$$

$$G^B(v) = \gamma v = \frac{x_n - x_{n-1}}{\Delta_t} \quad (\text{B.10})$$

Adding $G^F(v)$ and $G^B(v)$ we get

$$2 \times G(v) = \frac{x_{n+1} - x_n + x_n - x_{n-1}}{\Delta_t} \quad (\text{B.11})$$

$$\implies G(v) = \frac{x_{n+1} - x_{n-1}}{\Delta_t} \quad (\text{B.12})$$

Using this expression in eq [B.8](#), we get the final expressions for damped velocity verlet algorithm

$$x_{n+1} = x_n + \Delta_t v_n + \frac{1}{2} \Delta_t^2 a_n \quad (\text{B.13})$$

$$v_{n+1} = \frac{1}{1 + \Delta_t \gamma / 2m} [v_n (1 - \Delta_t \gamma / 2m) + \frac{\Delta_t}{2m} (F_{n-1} + F_n)] \quad (\text{B.14})$$

Appendix C

$E_{shoulder}$ versus time (t) for $\epsilon = 0.2$ and $\epsilon = 1.1$

To show that the $E_{shoulder}$ is independent of the value of strain (ϵ), we plotted the $E_{shoulder}$ versus time (t) graphs for higher ($\epsilon = 1.1$) and lower ($\epsilon = 0.2$) values of strains.

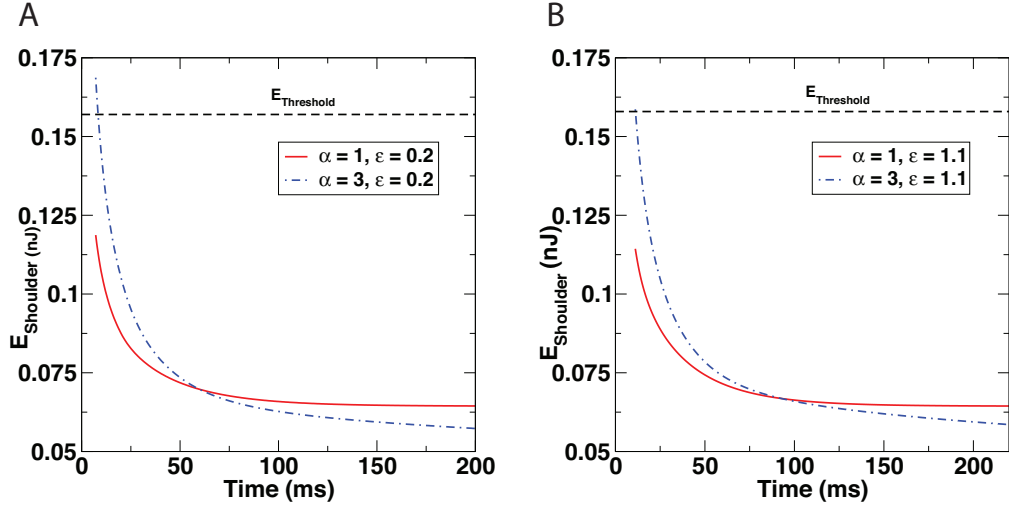


Figure C.1: **A.** $E_{shoulder}$ is plotted with time for lower strain of $\epsilon = 0.2$. **B.** $E_{shoulder}$ is plotted for a higher strain value of $\epsilon = 1.1$. Both **A** and **B** show $\alpha = 3$ model-Hydra is able to complete its motion due to $E_{shoulder} > E_{Threshold}$, regardless of the value of ϵ . $E_{shoulder}$ in **A** is higher than **B** because of lower initial energy dissipation which occurs during the contraction step.

Appendix D

Maxwell's model for Viscoelasticity

When a viscous fluid is subject to a shear stress, it responds by immediately dissipating the applied stress internally. While when the same shear stress is applied to an elastic material, it stores the stress energy and releases it back when such stress is removed. For viscous fluids, a shear stress (σ) is said to be proportional to strain rate while stress is directly proportional to strain in a completely elastic material. More rigorously, materials can be categorized

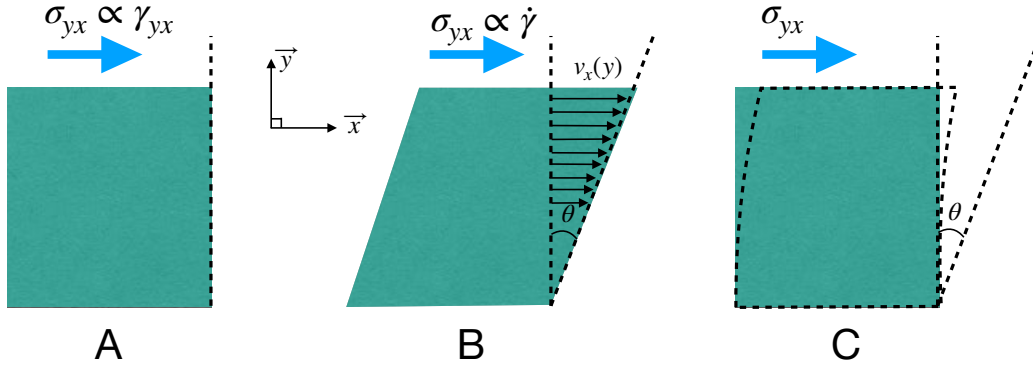


Figure D.1: **A.** A completely elastic solid undergoes a shear stress $\sigma_{yx} = \sigma_{xy}$. In such a case, the shear stress is directly proportional to shear strain. **B.** A completely viscous undergoes shear stress, and immediately dissipates it. In this case the shear stress is not proportional to the strain, but the strain rate. **C.** A material which is viscoelastic has a more complex response to shear stress. It has both storage as well as dissipative components.

based on the stress relaxation time (λ). A material with completely elastic response has an infinite stress relaxation time, or $\lambda \rightarrow \infty$, whereas a viscous

fluid, which does not store any stress energy has the stress relaxation time of $\lambda \rightarrow 0$. Based on such considerations, Maxwell proposed a two parameter phenomenological model to characterize a viscoelastic material. For the present case in fig [D.1](#), we can write the Maxwell's model in component form as

$$\sigma_{yx}(t) + \lambda \frac{\partial \sigma_{yx}(t)}{\partial t} = \eta \dot{\gamma}(t)_{yx} \quad (\text{D.1})$$

Here, λ is the stress relaxation time, σ_{yx} is the component of stress tensor co-planar to the top surface in fig [D.1](#), η is the constant determining the viscous contribution, while η/λ determines the elastic contribution. In the following sections, we will analyse different solutions to Maxwell's model.

D.1 Stress relaxation under constant strain of

$$\gamma_{yx}(t) = \gamma_{yx}^0$$

From fig [D.1](#) at time $t = 0$, a constant strain of $\gamma_{yx} = \gamma_{yx}^0$ is applied to the viscoelastic system. Putting this strain in the Maxwell's model, we get

$$\sigma_{yx}(t) + \lambda \frac{\partial \sigma_{yx}(t)}{\partial t} = \eta \frac{\partial \gamma(t)_{yx}}{\partial t} \quad (\text{D.2})$$

$$\implies \sigma_{yx}(t) + \lambda \frac{\partial \sigma_{yx}(t)}{\partial t} = 0 \quad (\text{D.3})$$

Using integrating factor, and the initial condition of $\sigma_{yx}(0) = G\gamma_{yx}^0$, we get

$$\sigma_{yx}(t) = G\gamma_{yx}^0 e^{-t/\lambda} \quad (\text{D.4})$$

$$\implies G(t) = \frac{\sigma_{yx}(t)}{\gamma_{yx}^0} = G e^{-t/\lambda} \quad (\text{D.5})$$

Here, $G(t)$ is defined as the stress relaxation modulus. From the above derivation, we can see that $G(t) \rightarrow \eta/\lambda$ as $\lambda \rightarrow \infty$, which is a completely elastic response. We also note that the relaxation modulus $G(t)$ is not a function of the 'strain' or its derivatives. This means that both low or high strains can be characterized by $G(t)$. This is a result of the Maxwell's model being linear. This linearity has been further exploited to create a generalized Maxwell's model. Such models are built to characterize materials with more than one relaxation mode. The relaxation modulus then is made up of a linear superposition of modulus of individual modes.

D.2 Stress relaxation under oscillatory strain: Strain of $\gamma_{\theta\phi} = \gamma_{\theta\phi}^0 \sin(\omega t)$

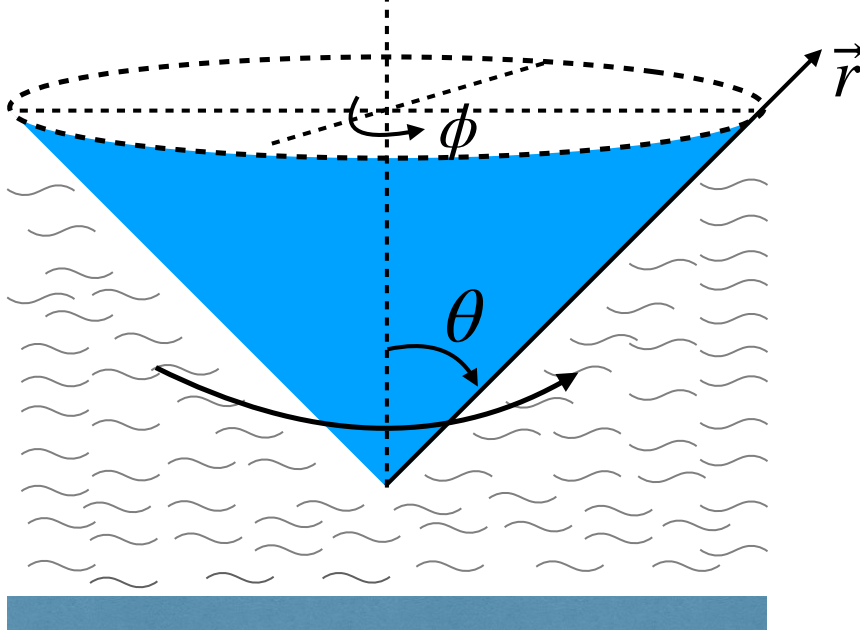


Figure D.2: Illustration of a cone and plate type Rheometer assembly. The cone rotates/oscillates along the ϕ direction. The oscillation frequency is kept to be low enough such that the fluid radially outward forces can be ignored.

Here, we solve the Maxwell's model for a cone and plate Rheometer geometry (fig [D.2](#)). The cone is lowered in a viscoelastic fluid and oscillates along the ϕ direction. We use spherical coordinates for ease of calculation. From observation, we can see that the most important component of stress is the $\sigma_{\theta\phi}$ component. We first write the Maxwell's model for this component as

$$\sigma_{\theta\phi}(t) + \lambda \frac{\partial \sigma_{\theta\phi}(t)}{\partial t} = \eta \frac{\partial}{\partial t} [\gamma_{\theta\phi}^0 \sin(\omega t)] \quad (\text{D.6})$$

From observing the geometry, we can say that the most significant component of velocity in this case is v_ϕ . By symmetry, and the fact that the fluid is in-

compressible, we note that v_ϕ is a function of θ and \vec{r} only. At $\theta = \pi/2$, which the bottom of the cone, fluid does not have any motion, thus $v_\phi(\theta \rightarrow \pi/2, r) \rightarrow 0$.

Due to the linear nature of Maxwell's model, we also know that the frequency of the measured shear stress would be the same as the applied strain, and the difference would only be in a phase. With this in mind, we can directly say that a general solution for stress in this situation would be

$$\sigma_{\theta\phi} = \sigma_{\theta\phi}^0 \sin(\omega t + \delta) \quad (\text{D.7})$$

Using the properties of trigonometric functions, this can be expanded as

$$\sigma_{\theta\phi} = G'(\omega) \sin(\omega t) + G''(\omega) \cos(\omega t) \quad (\text{D.8})$$

If we put this test function inside the differential equation, we can solve for G' and G'' . The stress-strain equation thus becomes,

$$\sigma_{\theta\phi} = \gamma_{\theta\phi}^0 \left[\frac{G\omega^2\lambda^2}{1 + \omega^2\lambda^2} \sin(\omega t) + \frac{G\omega\lambda}{1 + \omega^2\lambda^2} \cos(\omega t) \right] \quad (\text{D.9})$$

Where,

$$G' = \frac{G\omega^2\lambda^2}{1 + \omega^2\lambda^2} \quad (\text{D.10})$$

$$G'' = \frac{G\omega\lambda}{1 + \omega^2\lambda^2} \quad (\text{D.11})$$

The phase lag in the stress-strain relationship, defined in [D.7](#) can be explicitly defined now as

$$\delta = \tan^{-1} \left(\frac{1}{\omega\lambda} \right) \quad (\text{D.12})$$

The $\tan(\delta)$, which is equal to G''/G' is also known as "loss tangent". The terminal responses of G' and G'' show that as $\omega \rightarrow 0$, $G' \propto \omega^2$, while $G'' \propto \omega$. Also, as ω becomes large, $G' \rightarrow G$ while $G'' \rightarrow \omega^{-1}$. The terminal responses naturally lead to the definition of a cross-over frequency as $\omega_c = 1/\lambda$. When $\omega \ll \omega_c$, we have a mostly viscous dominated phase, whereas when $\omega \gg \omega_c$, G' plateaus off, and we have a completely elastic phase.

In the solutions above, G' is known as the storage modulus, as it characterizes the elastic response of the material. This is in-phase with the externally imposed strain. The G'' is known as the loss modulus, which characterizes the viscous response. From the equation [D.9](#), we can see that G'' is associated with $\cos(\omega t)$, which is exactly 90° out phase with the stress, thus being proportional to strain rate.

D.3 Stress relaxation under oscillatory strain rate: Strain rate of $\dot{\gamma}_{\theta\phi} = \dot{\gamma}_{\theta\phi}^0 \sin(\omega t)$

Following along similar arguments as section [D.2](#) when we apply an oscillatory strain rate of $\dot{\gamma}_{\theta\phi} = \dot{\gamma}_{\theta\phi}^0 \sin(\omega t)$, the stress response is captured by a phase lag of ϕ , and can be written as $\sigma_{\theta\phi} = \sigma_{\theta\phi}^0 \sin(\omega t + \phi)$. Expanding this using the trigonometric identities and putting the guess solution back in the Maxwell's model, we get

$$\sigma_{\theta\phi} = \dot{\gamma}^0 \left[\frac{\eta}{1 + \omega^2 \lambda^2} \sin(\omega t) - \frac{\eta \omega \lambda}{1 + \omega^2 \lambda^2} \cos(\omega t) \right] \quad (\text{D.13})$$

In this case, we define η' as $\frac{\eta}{1 + \omega^2 \lambda^2}$ and η'' as $\frac{\eta \omega \lambda}{1 + \omega^2 \lambda^2}$. η' is known as "dynamic viscosity" of the material. It can be seen that η' is associated with the part of eq [D.13](#) where $\sigma_{\theta\phi}$ is directly proportional to the strain rate, while η'' is associated with the part which is 90° out of phase with the strain rate.

We can therefore see that multiple different moduli can be used to characterize both the viscous and the elastic response of the material. From [D.2](#) and [D.3](#) we can see that in an "oscillatory strain" mode of the rheometer, the quantities G' and G'' characterize the elastic and the viscous response of the given material, while in the "oscillatory strain rate" mode, it is the "dynamic viscosity" or " η'' ", which is responsible for characterizing the viscous response, and η' for the elastic.